Modeling the Ice Pump under Antarctic ice shelves.

Diploma Thesis
at the
Leibniz Institute for Baltic Sea Research
Department of Physical Oceanography and Instrumentation
by Felix Franz Josef Hellfried Buck.
University of Rostock
Faculty of Mathematics and Natural Sciences
Institute of Physics

Supervisor and First Reviewer: Hans Burchard[1]
Second Reviewer: Lars Umlauf[1]

[1] Leibniz-Institute for Baltic Sea Research, Rostock-Warnemünde, Germany

Declaration According to the Examination Regulations §17(5)

I hereby declare that I have written this thesis without any help from others, besides changes to the code of GETM, providing a domain using rigid lid, written by Knut Klingbeil. I further declare that I have used no sources and auxiliary means, other than those mentioned.

Rostock, June 2014 Felix Franz Josef Hellfried Buck.

The following programs were used:

- GETM and GOTM: The programs used to model the ice shelf.
- MATLAB: Creating/reading netCDF files and preparing data output.
- Inkscape: Finalizing the output and figures.
- GIMP: Used to finalize large map figures that were rendered in chunks by MATLAB.
- Linux using the Ubuntu distribution: Operating system of the computer.
- Kile: Writing this document.
- minor auxiliary programs such as text editors, git and svn version control.

The recommended renderer of the electronic *.pdf version is Ghostscript.

Contents

1 Antarctic ice shelves

Antarctic ice shelves are the floating extensions of the antarctic ice sheet [12] generally observed over the continental shelf, thus constituting a cavern of sea water. The last contact of the ice sheet with the ground is named the grounding line, which is usually the deepest part of the ice shelf. From the grounding line outwards the ice shelf has an upward slope and ends at the calving front, named in reference to the calving of icebergs. Ice shelves compose nearly 15% of the Antarctic ice sheet and constitute half the coastline of Antarctica [16,31]. Fig. 1 displays Antarctica, including the Southern Ocean and marginal seas, locations of ice shelves and ice sheet elevation. Bedrock topography of the same region, including grounding, coast and calving lines are pictured in fig. 2. The mass of the Antarctic ice sheet has it's source in snow accumulation in the interior of the continent and discharges, in numerous ice streams along the bedrock topography into the ocean [3]. Of the Antarctic ice mass, an estimated 60% to 80% flow through ice shelves [10,39] and ice sheet mass loss is approximately evenly shared between melting at the ice shelf base and iceberg calving; however, for individual ice shelves the ratio of basal melting and calving can vary significantly, e.g. the largest Antarctic ice shelves (Ross and Ronne-Filchner) loose 83% of their mass to calving and contribute $1/3$ of total Antarctic iceberg production. In contrast, smaller ice shelves near the Bellingshausen and Amundsen Sea, like George IV, Getz, Totten and Pine Island, attribute 74% of their mass loss to basal melting, and an ice shelf area comprising 91% of the total ice shelf area only produces half of the total basal mass loss [3]. Warmer ocean waters reaching ice shelves with high melt rates are therefore the main factor of inland ice sheet dynamics [10] and a collapse of the whole West Antarctic ice sheet would result in an global mean sea level rise of about 3.3 m [11]. Hellmer et al. [8] present results of a regional ice-ocean model coupled to outputs from climate models which show that, by the end of the twenty-first century, the Ronne-Filchner cavern will be filled with warm water from the Weddel sea gyre, leading to a twentyfold increased basal mass loss with major consequences regarding the stability of the Western Antarctic ice sheet. While anthropogenic climate change leads to increased snow accumulation and inland precipitation, the Antarctic ice sheet will be a net contributor to global sea level rise and for the strongest warming scenario Winkelmann et al. [45] predict a dynamic ice sheet loss of 1.25 m in the year 2500.

Table 1: Marginal seas of the Southern Ocean, as illustrated in fig. 1.

Number	Name	Number	Name
1	Weddell Sea	2	Lazarev Sea[1]
3	Riiser Larsen Sea[1]	4	Cosmonauts Sea[1]
5	Coorperation Sea	6	Davis Sea[2]
7	Tryoshnikova Gulf	8	Mawson Sea
9	Dumont d'Urville Sea	10	Somov Sea
11	Ross Sea	12	McMurdo Sound
13	Amundsen Sea	14	Bellingshausen Sea
15	Drake Passage	16	Bransfield Strait

[1] Norway recognizes the Lazarev, Riiser Larsen and parts of the Cosmonauts Sea as the Kong Håkon VII Hav Sea.

[2] The 55th circular letter of the IHB [13] addresses the inconsistency in the draft of the 4th edition of S-23 [14], for the westward limit of the Davis Sea, i.e. fig. 1 uses coordinates according to the majority view of Australia, which is supported by the United Kingdom and dismisses the Russian proposal.

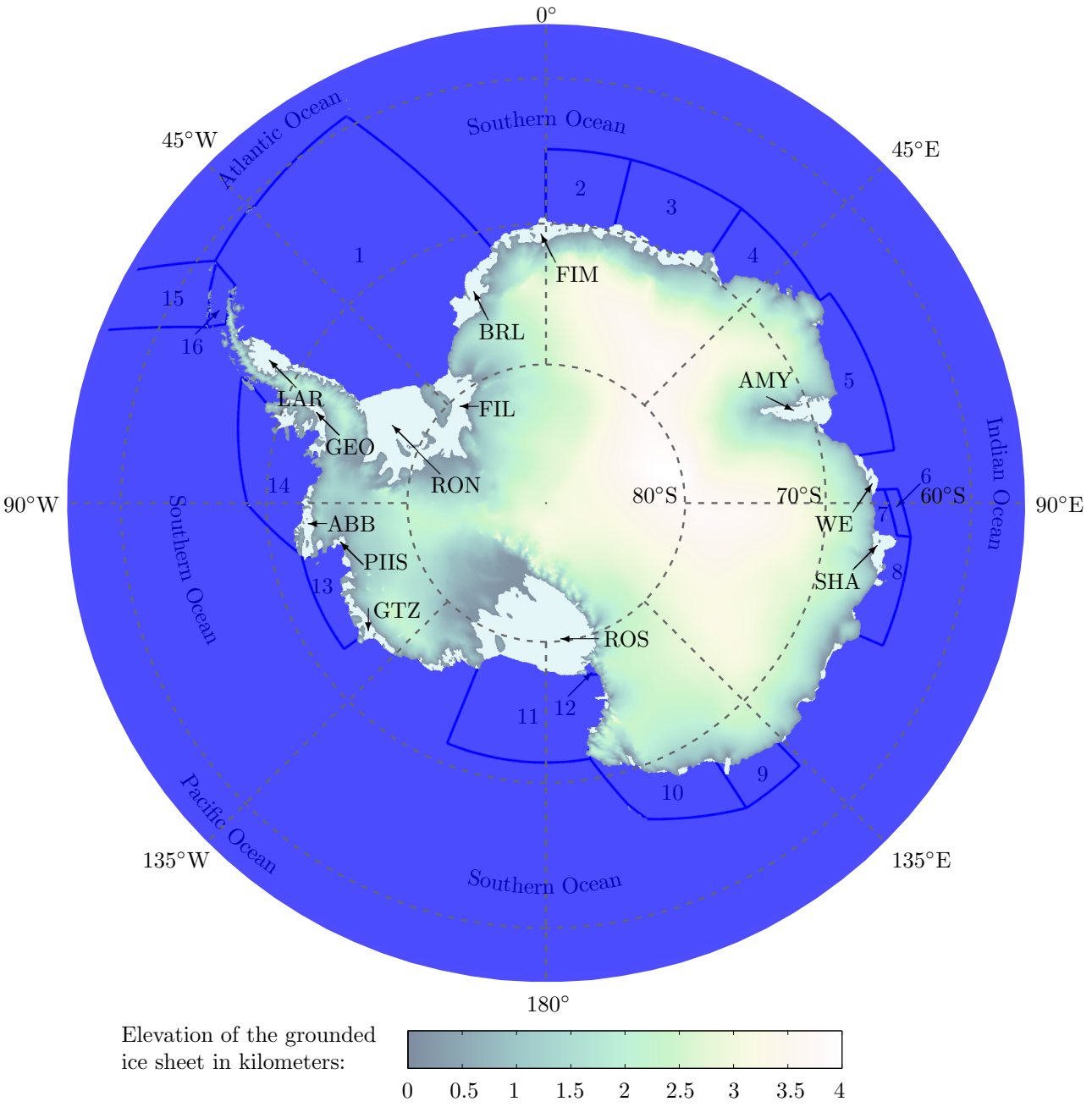

Figure 1: A map of Antarctica and the Southern Ocean, including the ice sheet[42], selected ice shelves[42] and marginal seas[14]. Ice shelf acronyms are listed in table 4 and the marginal seas are referenced in table 1.

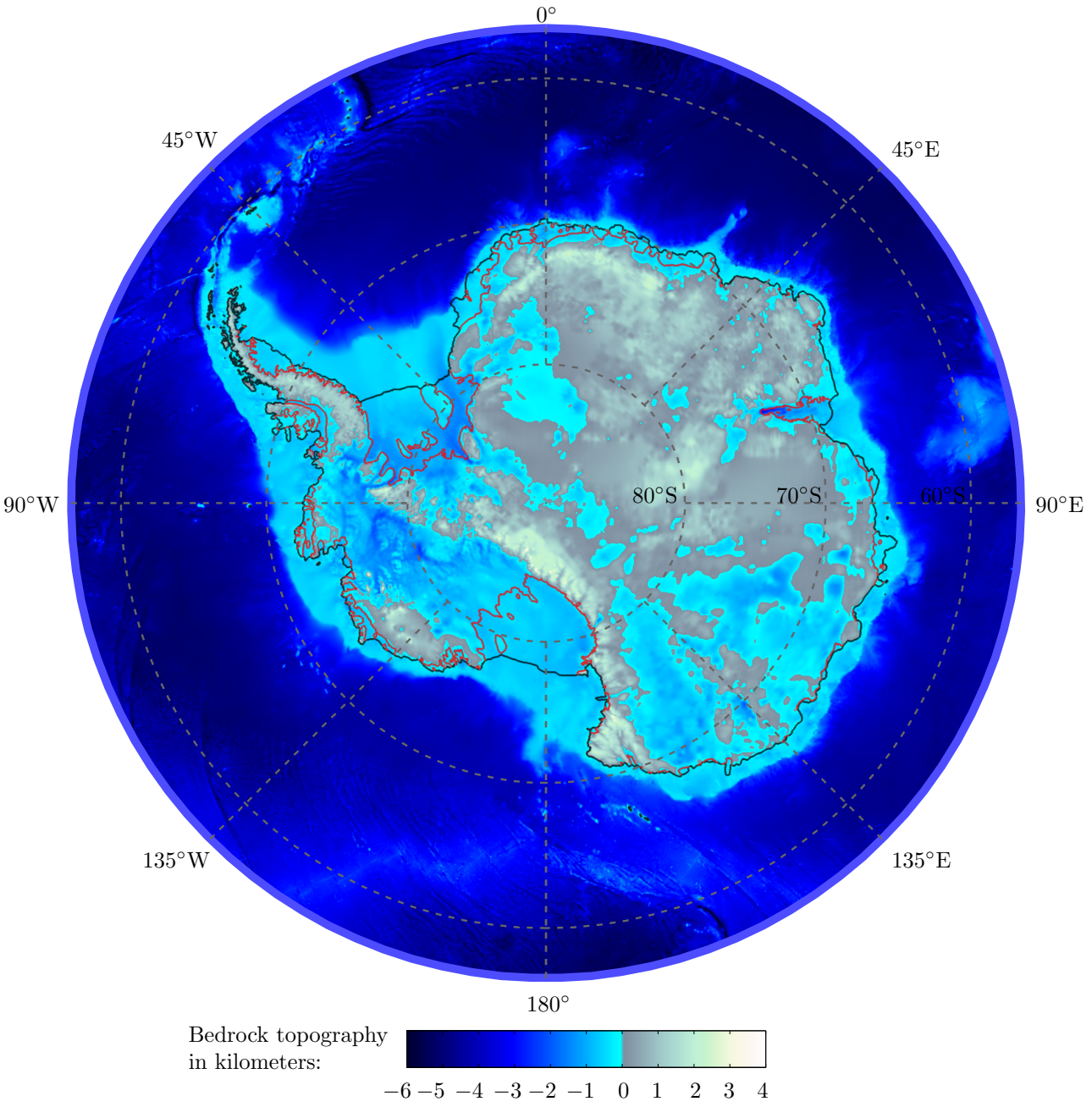

Figure 2: The bedrock topography [42] of Antarctica and the Southern Ocean, with coast and calving lines as a black contour and grounding lines as red contours.

1.1 Dynamics inside Antarctic ice shelf caverns

The freezing point of sea water is dependent on salinity and pressure[15,27,30], thus water at the in-situ surface freezing point is capable of melting ice in greater depths. The basic characteristics of the circulation beneath ice shelves were first described by Robin[35]: Cavern water melts the ice shelf near the grounding line and gets fresher and colder in the process, forming buoyant Ice Shelf Water (ISW). The general factors affecting the path that the ISW takes are cavern topography, Coriolis force, buoyancy, basal friction and entrainment of surrounding cavern water[39]. Vertically, the ISW follows the upwards slope of the ice shelf and may become supercooled, thus forming frazil ice that can be deposited at the ice shelf base as a slushy layer whose consolidation creates marine ice, in parts up to 350 m thick[39]. If ISW reaches a depth of neutral buoyancy, it can separate from the ice shelf base. Frazil ice deposition in addition to basal freezing, thus redistributes ice mass underneath the ice shelf, this was later coined the 'Ice Pump' by Lewis and Perkin[25]. Back at the grounding line ISW is replaced by cavern water which is formed from subglacial freshwater (SFW)[19,31] mixed with High Salinity Shelf Water (HSSW) or intrusion of Circumpolar Deep Water (CDW)[3]. This forces a thermohaline circulation[31,35] within the ice shelf cavern. Additionally to melting near the grounding line, high seasonal melt rates can occur near the calving front, due to tidal and wind-induced mixing as well as warming of the water column in summer[3,5]. Leaving the calving front behind, formation of polynyas[24] and sea ice[5] production off the calving front is increased by ISW, especially if ISW transports frazil ice out of the cavern. This leads to formation of HHSW, due to brine rejection. HSSW can circulate back into the cavern or form Antarctic Bottom Water (AABW), whose descend to the ocean abyss and is a key component of the global thermohaline circulation[5,10,22,31]. The basic Ice Pump is pictured in fig. 3 and fig. 4 displays the current understanding.

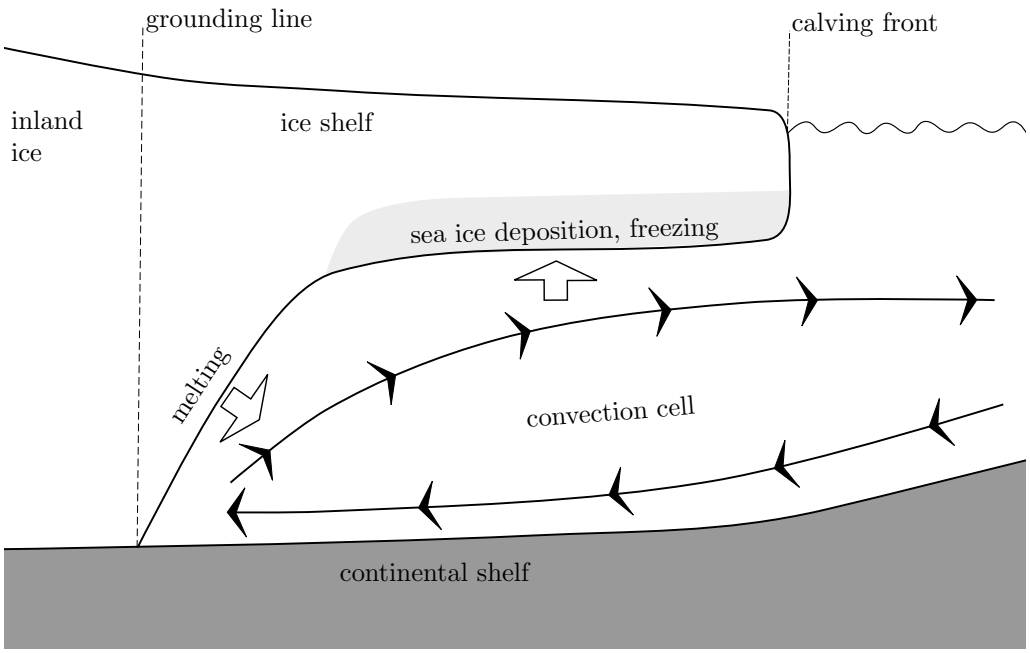

Figure 3: A schematic view of an antarctic ice shelf cavern, similar to the proposed convection cell by Robin[35].

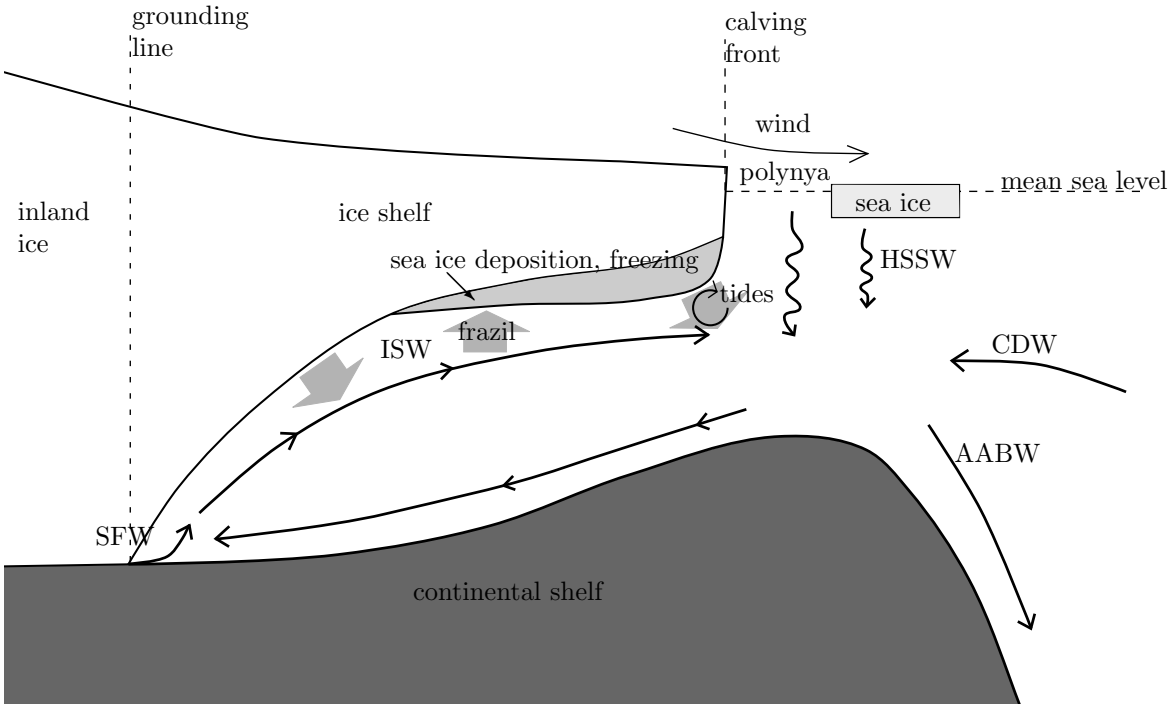

Figure 4: Schematic of processes in and around Antarctic ice shelves, as described in 1.1. Filled, gray arrows indicate melting (arrow pointing to the cavern) and freezing (arrow pointing to the ice shelf) regimes. Caverns with intrusion of warm CDW usually lack a freezing regime.

1.2 Morphologies of selected Antarctic ice shelves

This section displays bedrock topography[42] of various ice shelves for the interested reader. The employed color scheme is the same as is used in fig. 2. To visualize the actual cavern geometry, the ice shelf draft and bathymetry is transected and the vertical cavern profiles along those transects are displayed. Finally, a small section of the Antarctica is provided, detailing the location of the cavern.

Fig. 5, shows PIIS, one of the rapid thinning ice shelves in the Amundsen Sea sector[3,17]. PIIS is therefore extensively studied. Jenkins et al.[21] employed an autonomous underwater vehicle (AUV) sampling water properties in the ice shelf cavern. Along it's path the AUV found a distinct ridge in the bathymetry, which can be seen in the upper right of fig. 5 at about 32 to 42 km distance to the 2010 grounding line. Satellite images of PIIS from the early 1970s show bumps in the ice shelf and Jenkins et al.[21] conclude that the ridge was a former grounding line, which was then still in partial contact with the ice shelf. While providing invaluable data of cavern water properties, this finding also confirmed the suspicion of accelerating grounding line retreat along a downwards inland slope of the bedrock topography[37]. The ice shelf can only be expected to stabilize, as a result of changing inflow conditions, massive increase in inland precipitation feeding the ice shelf or a change of the slope going further inland. While PIIS observed a slowing of it's thinning and basal melting was reduced by 50% between January 2010 and 2012, Dutrieux et al.[4] attribute this change to a strong La Niña event and expect PIIS to return to it's earlier melting rates.

Fig. 6 pictures FIM, an ice shelf near the Weddel and Lazarev marginal seas. A special characteristic of FIM is the extension of the ice shelf over the abyss. Using POLAIR (Polar Ocean Land Atmosphere and Ice Regional) model Smedsrud et al.[40] showed warm CDW intrusion into the Jutul basin (At ca. 70 to 140 km distance to the grounding line in the upper right picture of fig. 6.) below FIM, caused by continental upslope Ekman pumping or interactions with the mean flow over the topography.

Fig. 7 shows the LAR cavern. Like it's smaller neighbors LarsenA and LarsenB, LAR is one of most northwards located ice shelves; however, unlike LarsenA and LarsenB it has not collapsed yet, although collapse is predicted at the end of the next century, if current thinning rates continue[32].

Fig. 8 depicts AMY, the third largest and deepest ice shelf in Antarctica[6]. In contrast to PIIS, FIM and LAR, the AMY ice shelf cavern is characterized by inflowing HSSW, constituting a cold cavern, hence producing frazil ice in the rising ISW. The ratio of direct basal freezing to frazil ice deposition is 2.3, according to models of Galton-Fenzi et al.[6].

Fig. 9 shows ROS, the largest Antarctic ice shelf[3].

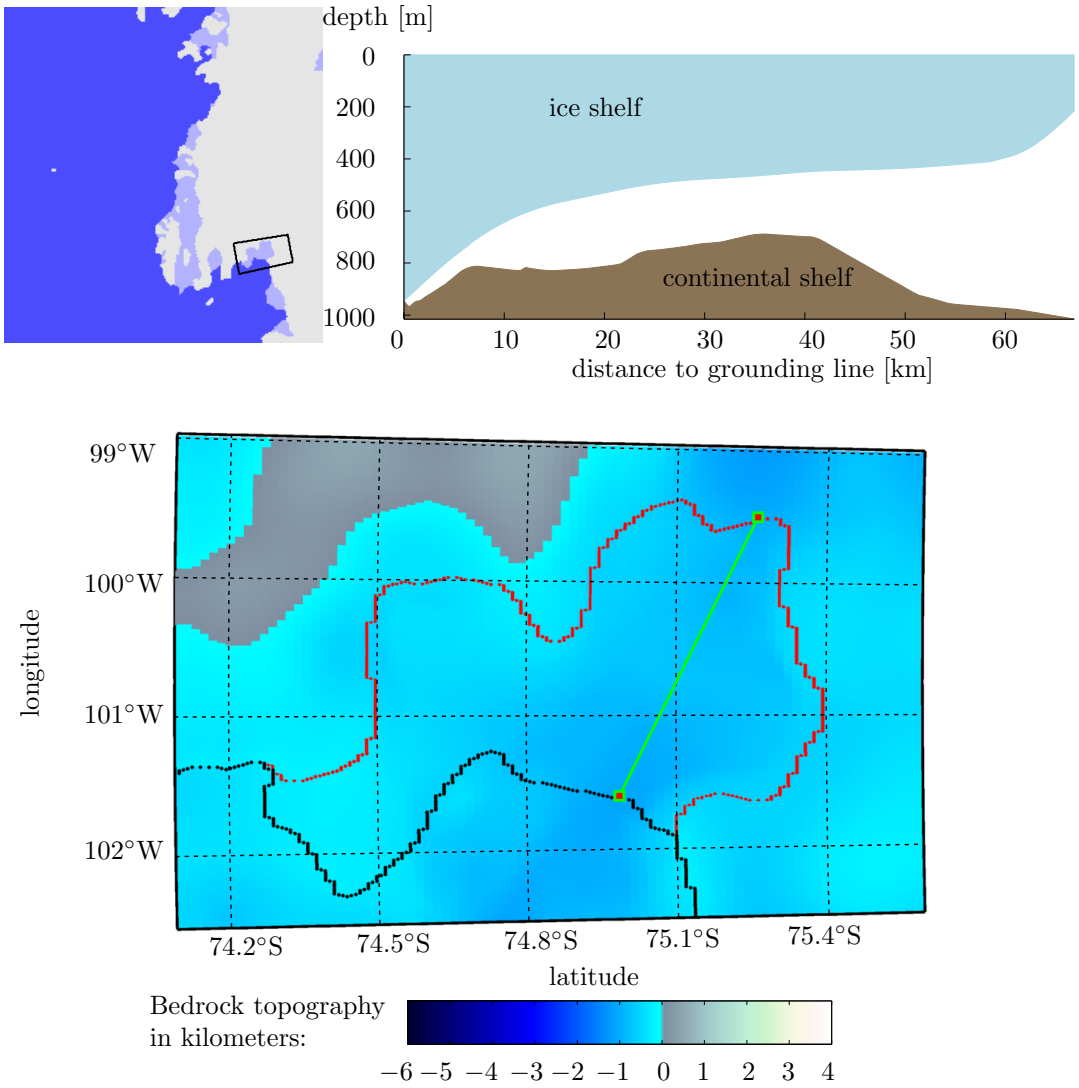

Figure 5: The Pine Island ice shelf[42].
Bottom: Bedrock topography of PIIS, with a transect in green, the coast and calving lines as a black contour and grounding lines as red contours.
Upper left: The location of the shown section within Antarctica, with grounded ice in white, ice shelves in pale blue and the Southern Ocean in blue.
Upper right: Vertical profile of the ice shelf draft and bathymetry along the transect.

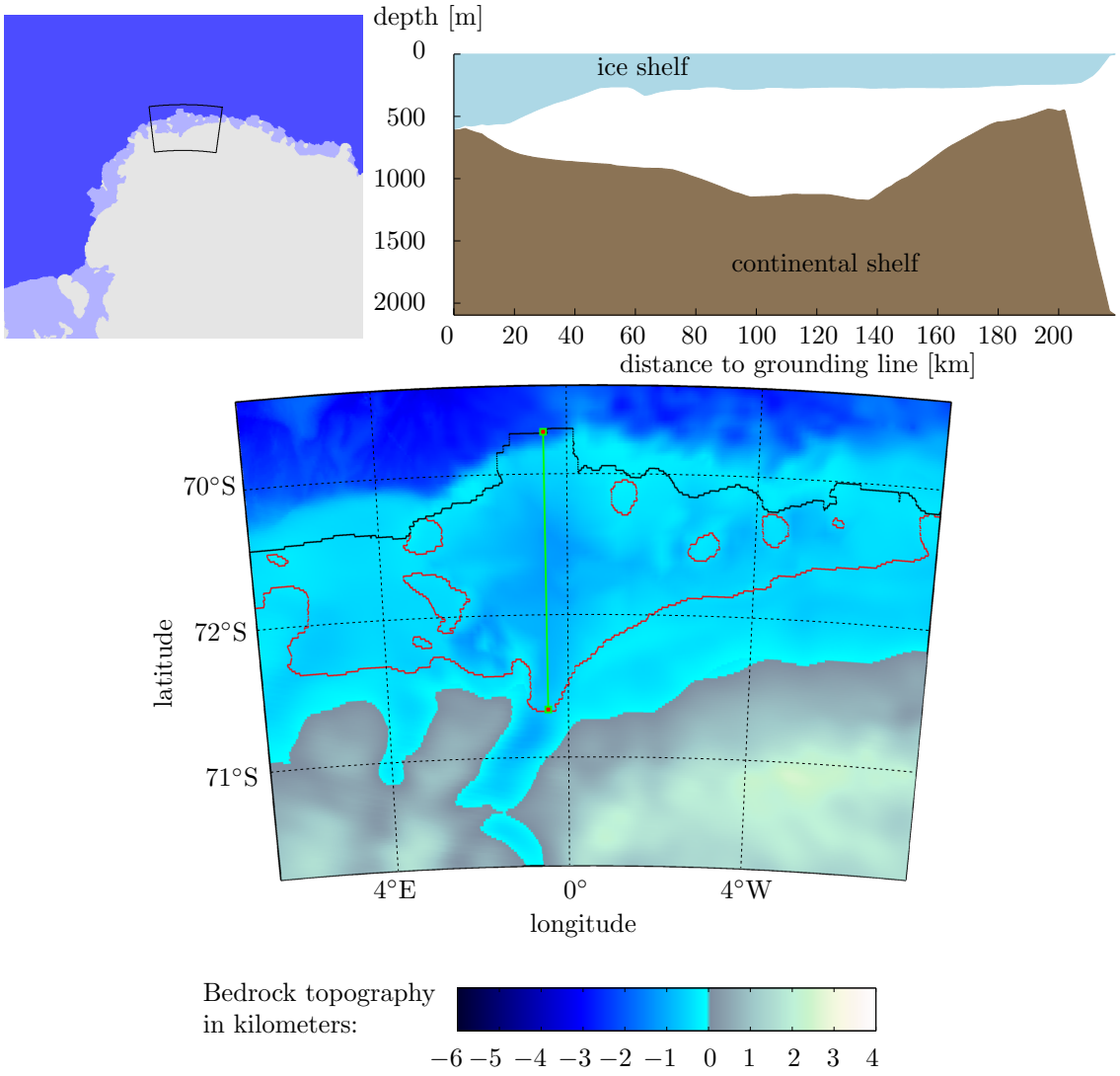

Figure 6: The Fimbulisen ice shelf[42].
Bottom: Bedrock topography of FIM, with a transect in green, the coast and calving lines as a black contour and grounding lines as red contours.
Upper left: The location of the shown section within Antarctica, with grounded ice in white, ice shelves in pale blue and the Southern Ocean in blue.
Upper right: Vertical profile of the ice shelf draft and bathymetry along the transect.

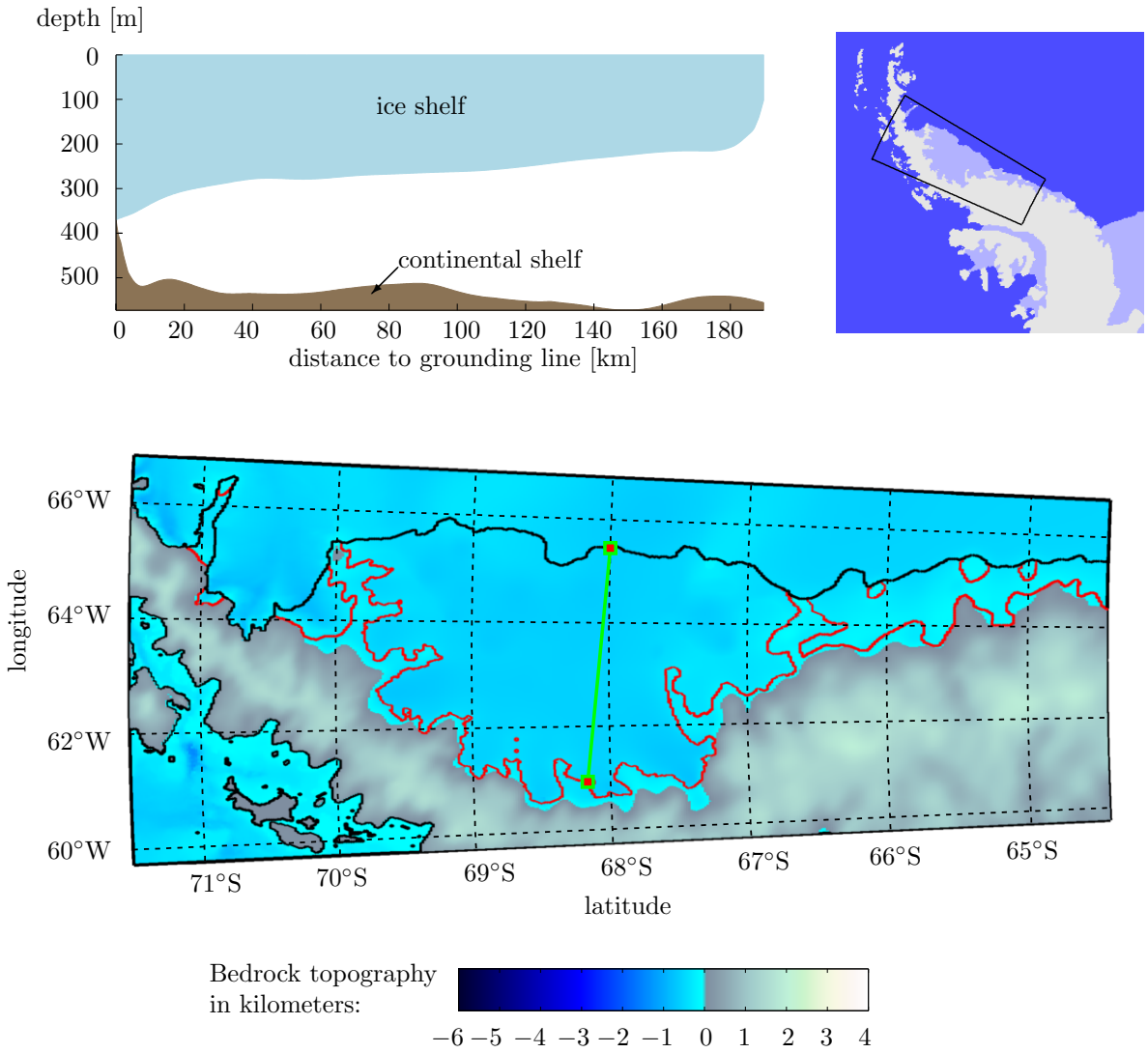

Figure 7: The Larsen C ice shelf[42].
Bottom: Bedrock topography of Larsen C, with a transect in green, the coast and calving lines as a black contour and grounding lines as red contours.
Upper left: Vertical profile of the ice shelf draft and bathymetry along the transect.
Upper right: The location of the shown section within Antarctica, with grounded ice in white, ice shelves in pale blue and the Southern Ocean in blue.

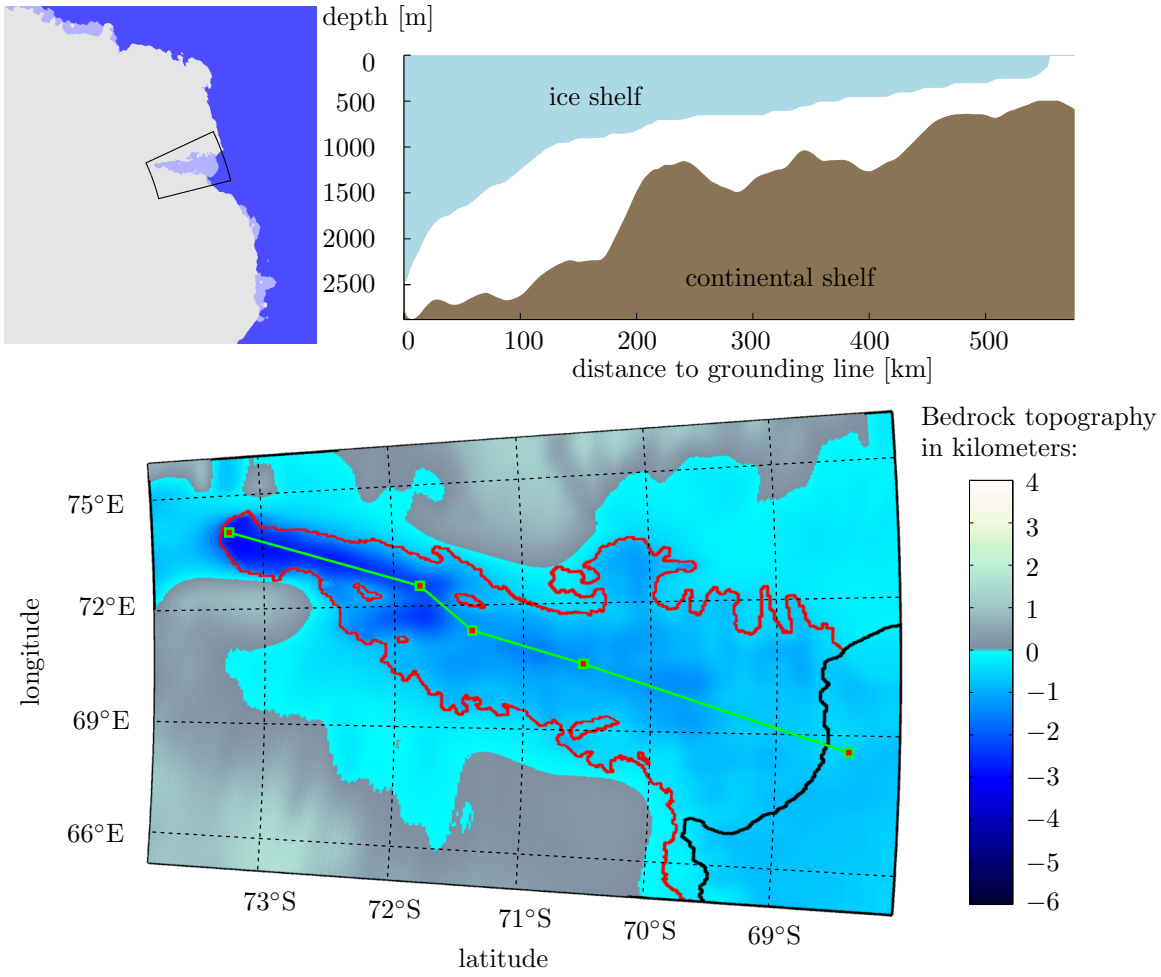

Figure 8: The Amery ice shelf[42].
Bottom: Bedrock topography of AMY, with a transect in green, the coast and calving lines as a black contour and grounding lines as red contours.
Upper left: The location of the shown section within Antarctica, with grounded ice in white, ice shelves in pale blue and the Southern Ocean in blue.
Upper right: Vertical profile of the ice shelf draft and bathymetry along the transect.

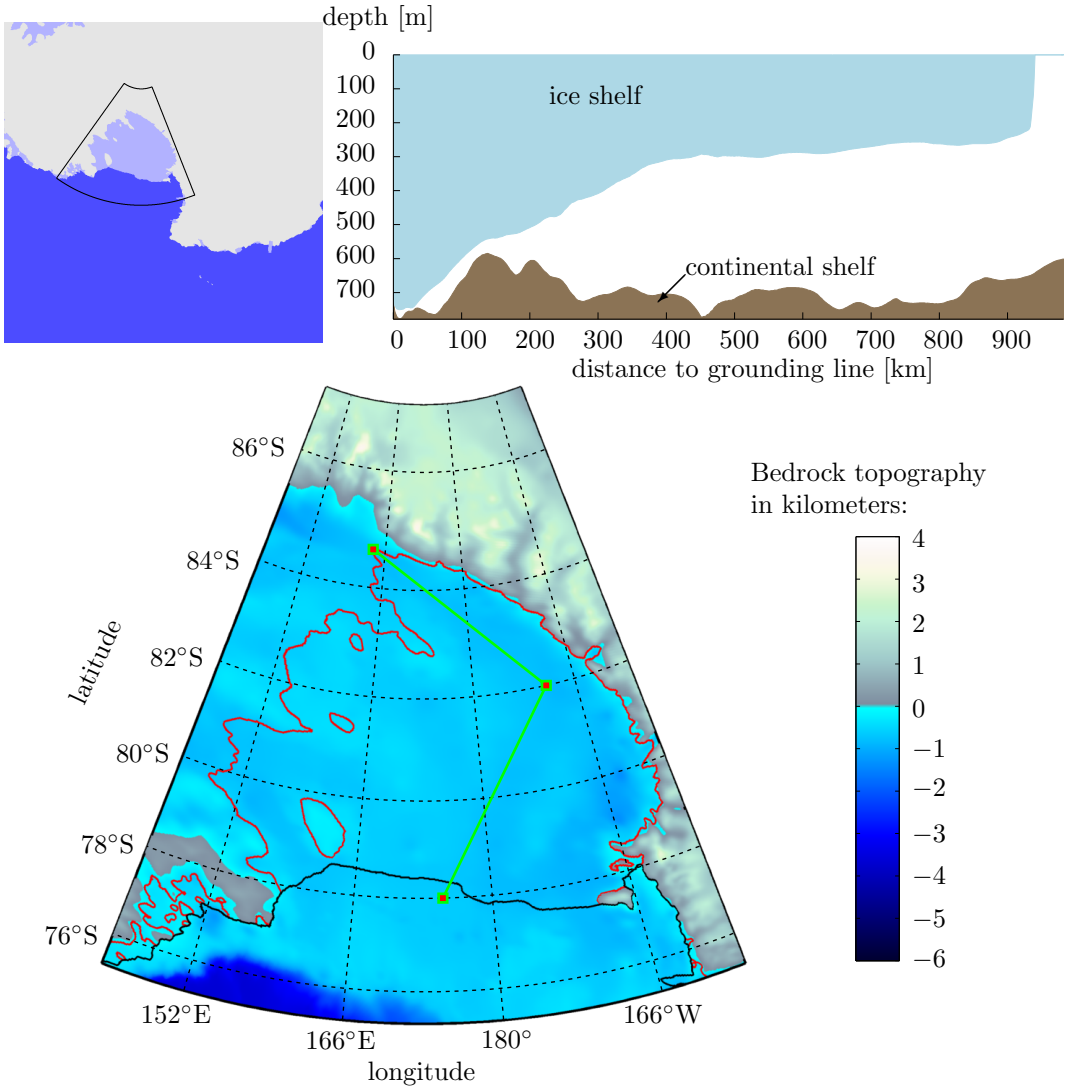

Figure 9: The Ross ice shelf[42].
Bottom: Bedrock topography of ROS, with a transect in green, the coast and calving lines as a black contour and grounding lines as red contours.
Upper left: The location of the shown section within Antarctica, with grounded ice in white, ice shelves in pale blue and the Southern Ocean in blue.
Upper right: Vertical profile of the ice shelf draft and bathymetry along the transect.

2 Parameterization of basal melting

The heat and salt fluxes at the ice-ocean interface, as shown in fig. 11, can be derived by examination of heat and salt conservation. The turbulent heat flux through the ice-ocean boundary layer ϕ_B^T is therefore equal to the sum of the conductive heat flux through the ice shelf ϕ_I^T and the latent heat flux ϕ_M^T caused by either melting or freezing; in comparison, the geothermal heatflux from the sea bed into the ice shelf cavern is much smaller and is usually ignored[36]. Any two phases of water are in thermal equilibrium during a first order phase transition; therefore, the temperature at the base of the ice shelf T_b is equal to the freezing point of seawater T_f. This leads to a typical ice shelf temperature profile with a low surface and a comparatively high basal temperature, e.g. fig. 10 shows an ice core of the Antarctic ice sheet near Byrd Station with a pressure melting point of -1.5 °C. Correspondingly to the heat fluxes, the salt flux through the ice-ocean boundary layer ϕ_B^S is equal to the salt flux ϕ_M^S due to either salt loss in case of melting or gain in case of freezing. There is no equivalent salt flux to ϕ_I^T, given that a strong desalination process is taking place when sea water freezes, i.e. all components of the ice shelf (the extended ice sheet, ice created through direct basal freezing and frazil deposition) are assumed to have zero salinity[9]. With these considerations the following 'three equation formulation' can be deduced:

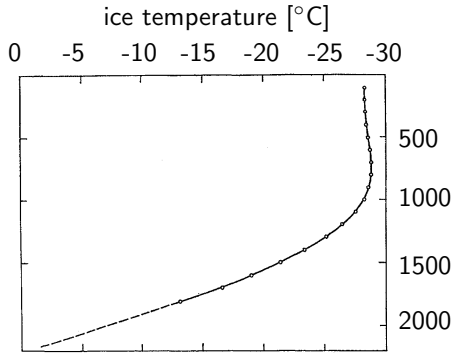

Figure 10: Drill hole temperature profile, as reported by Ueda and Garfield[43]. The vertical axis is the depth below the 1968 surface in meters.

$$\phi_B^T = \phi_M^T + \phi_I^T, \tag{1}$$
$$\phi_B^S = \phi_M^S, \tag{2}$$
$$T_f = T_f(S,p) = T_b. \tag{3}$$

This formulation was used by various authors[7,10,18–20,22,33], although they employed different approaches concerning ϕ_I^T and the parametrization of turbulent exchange coefficients in ϕ_B^T and ϕ_B^S. Secondly the process of freezing is different than the melting process, as described in the introduction, frazil ice forms in supercooled water and is deposited at the ice shelf base in addition to direct freezing, thus arises a need for a different formulation in case of freezing. In accordance with Hellmer and Olbers[7] the latent heat and salt fluxes ϕ_M^T and ϕ_M^S can be written as:

$$\phi_M^T = -\rho_I m L, \tag{4}$$
$$\phi_M^S = -\rho_I m S_b. \tag{5}$$

With ρ_I being the density of ice, L the latent heat of fusion and m the melting rate ($m > 0$ corresponds to a melting and $m < 0$ to a freezing regime).

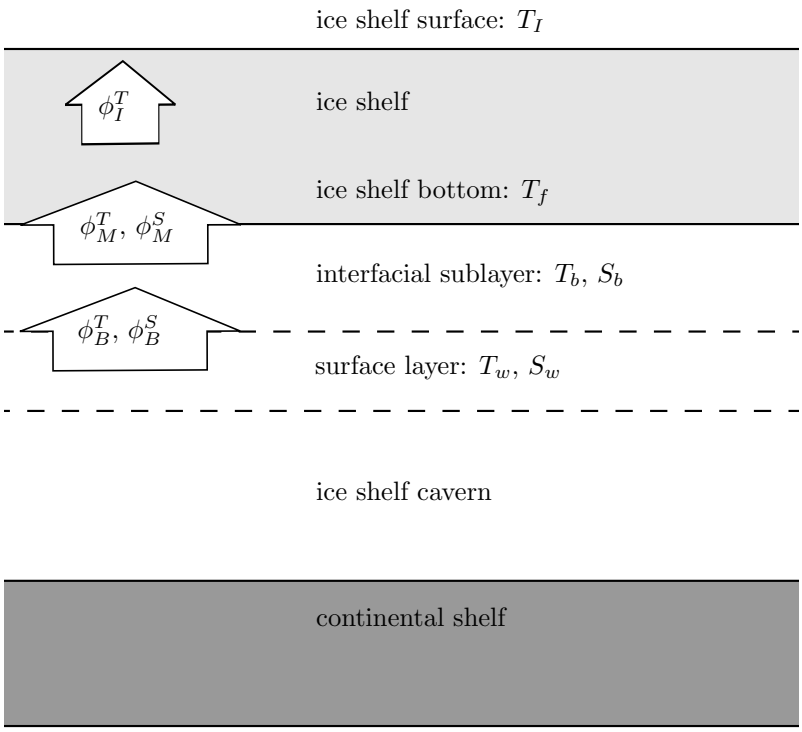

Figure 11: The fluxes, temperatures and salinities in an Antarctic ice shelf cavern, as used in this document. The direction of the fluxes is dependent on ice shelf melting or seawater freezing. The ice-ocean boundary layer and it's subdivisions (the interfacial sublayer, surface and outer layer) are discussed in 2.2 and pictured in fig. 12.

The following sections are dedicated to the remaining fluxes of the 'three equation formulation':

- 2.1 presents different parametrizations of the heatflux into the ice shelf ϕ_I^T.
- 2.2 provides a framework for the ice-ocean boundary layer and double diffusion before listing different approaches concerning the turbulent fluxes $\phi_B^{T,S}$.
- 2.3 provides the parametrization of the drag coefficient and surface friction velocity.
- 2.4 discusses varying options to calculate the freezing point of seawater T_f.
- 2.5 summarizes the chosen parametrizations and displays melting rates under varying conditions.
- 2.6 discussed problems that arise from the theory.

2.1 The heat flux into the ice shelf

The treatment of the conductive heat flux through the ice shelf ϕ_I^T is problematic because temperature gradients within an ice shelf are generally not known. Exceptions are profiles from ice core drilling sites, which grant only small samples compared to the whole ice shelf area. Secondly, the slow moving ice shelf can not be treated as stationary, because the heat conduction process is slow in contrast to the other heat fluxes[33]; finally, the pace of melting differs from the slower process of freezing [Hellmer pers. com.]. There are several attempts, short of ignoring this flux, that deal with those issues and are outlined below.

2.1.1 Heat conduction using a linearized temperature gradient

Hellmer and Olbers[7] appraised the heat flux through the ice shelf using a linear temperature gradient and treated the ice shelf as stationary and arrived at the following approximation:

$$\phi_I^T = \rho_I c_I \kappa_I \frac{T_I - T_f}{D}.$$

With ρ_I being the density of ice, c_I the specific heat capacity of ice, D the ice shelf thickness, T_I the temperature at the ice shelf surface, T_f the temperature at the ice shelf base and κ_I the heat diffusion coefficient of ice at $-20°C$.

2.1.2 Heat conduction using constant vertical advection

Holland and Jenkins[9] allowed vertical advection in the ice shelf with a constant vertical velocity. They arrived at a similar expression to Hellmer and Olbers[7] but with an additional factor Π which was approximated to:

$$\Pi = \begin{cases} \frac{\omega_I D}{\kappa_I} & \text{for } m > 0 \\ 0 & \text{for } m \leq 0, \end{cases}$$

with ω_I being the vertical velocity of the ice shelf.

2.1.3 Heat conduction in dependence on the melting rate

Nøst and Foldvik[33] assumed that freezing reduces the temperature gradient and set the heat conduction into the ice shelf to zero in case of freezing. Jenkins et al.[22] followed this approach in his suggested 'three equation formulation' and arrived at:

$$\phi_I^T = \begin{cases} \rho_I c_I m (T_I - T_f) & \text{for } m > 0 \\ 0 & \text{for } m \leq 0. \end{cases} \tag{6}$$

2.2 Parametrization of the turbulent exchange coefficients

Before ϕ_B^T, ϕ_B^S and the different parameterizations can be discussed, there has to be a consistent description of the ice-ocean boundary layer at the ice shelf base; therefore, the terminology of other authors will be adapted to match the terminology used by Jenkins et al.[22], displayed in fig. 12. For example Hellmer and Olbers[7] used an ice-ocean interface and Holland and Jenkins[9] used a boundary layer, with a thickness of the interfacial sublayer, adjacent to a mixed layer. ϕ_B^T and ϕ_B^S can now be written as[7,44]:

$$\phi_B^T = \rho_w c_w \gamma_T (T_b - T_w), \tag{7}$$

$$\phi_B^S = \rho_w \gamma_S (S_b - S_w). \tag{8}$$

With ρ_w being the reference density of seawater, c_w the specific heat capacity of seawater, T_w and S_w the temperature and salinity of the well mixed parts of the upper surface layer and T_b and S_b the temperature and salinity of the interfacial sublayer. The differences in the parameterizations of Hellmer and Olbers[7], Holland and Jenkins[9] and Jenkins et al.[22] are located in the parameterization of the turbulent exchange coefficients γ_T and γ_S.

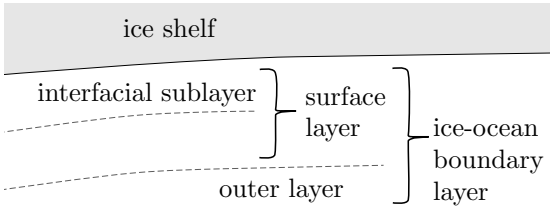

Figure 12: The subdivisions of the ice-ocean boundary layer according to Jenkins et al.[22]: The interfacial sublayer is a few millimeters to centimeters thick and the flow is determined by direct interactions with surface roughness and the transfer of momentum is ascertained through molecular viscosity. The surface layer extends a few meters and turbulent mixing is influenced by the adjacency of the boundary and the outer layer, which extends a few tens of meters where mixing is mainly affected by rotation and stratification.

2.2.1 Double diffusive processes

Double diffusive processes refer to the different molecular diffusivities of salt and heat in sea water, e.g. the molecular thermal diffusivity in cold seawater is about 200 times greater than salt diffusivity[29]. When ice melts at the base of the ice shelf the adjacent boundary layer might change in temperature much more quickly than in salinity; however, the salinity also determines the freezing point of seawater, thus affecting the melting rate and therefore plays an inhibiting role on the heat flux. The quotient of the thermal turbulent exchange coefficient and the haline turbulent exchange coefficient

$$R = \frac{\gamma_T}{\gamma_S} = \frac{\Gamma_T}{\Gamma_S}, \tag{9}$$

therefore describes the role of the limitation on the melting rate due to the slower diffusion of salt: If $R \gg 1$ then double diffusion needs to be accounted for, with the salinity slowing the diffusive process. Observations have shown that double diffusion usually plays a role in inhibiting the melting rate. Using laboratory studies as well as measurements under sea ice, McPhee[29] concluded that $35 \leq R \leq 70$ and Sirevaag[38] confirmed $R = 33$, for measurements under drifting Arctic sea ice in cases of rapid melting.

2.2.2 Constant turbulent exchange velocities

Hellmer and Olbers[7] set γ_T and γ_S to constant values, with the unit m s^{-1}, i.e. they are thermal and salinity exchange velocities, with:

$$\begin{aligned} \gamma_T &= 1 \cdot 10^{-4} [\text{m s}^{-1}], \\ \gamma_S &= 5.05 \cdot 10^{-3} \gamma_T. \end{aligned}$$

2.2.3 Turbulent exchange velocities in dependence on friction velocity

Jenkins[18] and Holland and Jenkins[9] introduced heat and salt transfer coefficients of the form:

$$\gamma_{(T,S)} = \frac{u_*}{2.12 \ln(u_* h/\nu) + 12.5(Pr, Sc)^{2/3} - 9}.$$

This formula was derived by Kader and Yaglom[23] for hydraulically smooth boundaries with u_* being the friction velocity, Pr and Sc the molecular Prandtl and Schmidt numbers, ν the kinematic viscosity of seawater and h the surface layer thickness. The friction velocity is parameterized with a quadratic drag law:

$$u_*{}^2 = C_d U^2. \tag{10}$$

with U being the free stream current beyond the interfacial sublayer and C_d a dimensionless drag coefficient. To account for de- or stabilizing effects of the buoyancy flux on the mixing within the upper surface layer Holland and Jenkins[9] expanded the equation in accordance to McPhee[28] to:

$$\gamma_{T,S} = \frac{u_*}{\Gamma_{Turbulent} + \Gamma^{T,S}_{Molecular}},$$

with:

$$\begin{aligned} \Gamma_{Turbulent} &= \frac{1}{k} \ln \left(\frac{u_* \xi_N \eta_*^2}{f h_\nu} \right) + \frac{1}{2 \xi_N \eta_*} - \frac{1}{k}, \\ \Gamma^{T,S}_{Molecular} &= 12.5(Pr, Sc)^{2/3} - 6. \end{aligned}$$

with k being the Kármán's constant, f the coriolis parameter, ξ_N a constant. The thickness of the interfacial sublayer is approximated to

$$h_\nu = 5 \frac{\nu}{u_*}.$$

The stability parameter η_* is written as:

$$\eta_* = 1 + \frac{\xi_N u_*}{f L_0 R_C},$$

with R_C being the critical flux Richardson number and L_0 the Obukhov length. The flux Richardson number is defined as

$$R_f = \frac{B \lambda}{u_*^3},$$

and has a critical value of $R_C \approx 0.2$ where turbulence no longer exists. B is the buoyancy flux and λ the mixing length. The Obukhov length is defined as

$$L_0 = \frac{u_*^3}{\kappa B}.$$

L_0 is positive if turbulence is suppressed by buoyancy and vice versa if L_0 is negative. For negative Obukhov lengths the stability parameter is set to 1, because it is assumed that frazil ice formation will have a stabilizing effect in case of freezing[9].

2.2.4 Variable turbulent exchange velocities with reduced complexity

Measurements of basal ablation and boundary layer water properties under the Ronne ice shelf were used to verify the complexity of previous parameterizations of the turbulent exchange coefficients. Jenkins et al.[22] proposed a simpler parameterization:

$$\gamma_{T,S} = u_* \Gamma_{T,S}, \tag{11}$$

with $\Gamma_{T,S}$ being analogous to thermal or haline Stanton numbers with dependence on the friction velocity instead of the velocity of the boundary flow, e.g. Γ_T can be written as

$$\Gamma_T \equiv \frac{\phi_B^T}{\rho_w c_w u_* [T_f - T_w]}.$$

$\Gamma_{T,S}$ are assumed to be constant and Jenkins et al.[22] proposed fixed values, by fitting their measurements of melting rates, temperatures, salinities and water velocities in the surface layer and setting R to values suggested by McPhee[29], see 2.2.1. Using constant turbulent exchange coefficients significantly reduces complexity compared to earlier parameterizations. The authors note that any deficiencies in the theory are included in the drag coefficient, because it is least constrained by independent observational evidence.

2.3 Parametrization of the drag coefficient and friction velocity

Using the 'law of the wall', the drag coefficient can be written as[29]

$$\sqrt{C_d} = \frac{\kappa}{\ln\left(\frac{d}{z_0}\right)}, \tag{12}$$

with κ being the Kármán's constant, d the distance from the boundary and z_0 the surface roughness length. According to McPhee[29] z_0 can be estimated with

$$z_0 \simeq \frac{1}{30} z_0^s. \tag{13}$$

z_0^s are the surface roughness features, which are generally unknown for ice shelves. Using sea ice as an estimate, surface roughness features can differ greatly between smooth freshly formed sea ice with roughness feature scales in a range of only sub-millimeters and older deformed sea ice with roughness feature scales of several centimeters[26,29]. It should be noted that the General Estuarine Transport Model (GETM) and the General Ocean Turbulence Model (GOTM) use a slightly different formulation[2] for d due to numerical discretization (tracer grid points are located between velocity grid points), i.e.

$$d = 0.5 \cdot z\text{'} + z_0, \tag{14}$$

with z' being the distance between the boundary and the nearest vertical grid point. Using (12), (13) and (14) the friction velocity (10) can be written as:

$$u_*^2 = \frac{\kappa^2}{\ln^2\left(\frac{0.5z\text{'}+\frac{1}{30}z_0^s}{\frac{1}{30}z_0^s}\right)} U^2. \tag{15}$$

2.4 The freezing point of seawater

To calculate the freezing point of seawater Jenkins et al.[22] suggested a linearized version of the formula introduced by Millero[30], i.e.

$$T_f \quad = \quad \lambda_1 S_b + \lambda_2 + \lambda_3 p, \tag{16}$$

with $\lambda_{(1,2,3)}$ being constants. It should be noted that the original formula[30] is slightly nonlinear in salinity and is strictly speaking only viable up to a pressure of 500 dbar, yet was applied throughout the literature[7,10,18–20,22,33] for greater pressures. With the arrival of the thermodynamic equation of seawater 2010 (TEOS-10), T_f can be calculated with greater accuracy and the formula is viable up to a depth of 10,000 m[15,27]. The derivation of the formula stems from the basic concept that the chemical potential of water in seawater at the freezing point is equal to the chemical potential of ice at the melting point:

$$\mu^W(S_A, T_f, p) \quad = \quad \mu^I(T_f, p). \tag{17}$$

S_A is the Absolute Salinity and is defined as:

$$S_A = S_R + \delta S_A = \frac{35.16504\text{g Kg}^{-1}}{35} S_p + \delta S_A(\phi, \lambda, p), \tag{18}$$

with S_R being the reference salinity, S_p the practical salinity and δS_A the absolute salinity anomaly. δS_A itself is dependent on latitude ϕ, longitude λ and pressure p. The Gibbs Seawater Oceanographic Toolbox fits (17) via the polynomial:

$$\begin{aligned} T_f \quad = \quad & c_0 + c_{23} S_A (c_1 + \sqrt{c_{23} S_A}(c_2 + \sqrt{c_{23} S_A}(c_3 + \sqrt{c_{23} S_A}(c_4 + \sqrt{c_{23} S_A}(c_5 + c_6 \sqrt{c_{23} S_A}))))) \\ & + c_{24} p (c_7 + c_{24} p (c_8 + c_9 c_{24} p)) \\ & + c_{23} S_A c_{24} p (c_{10} + c_{24} p (c_{12} + c_{24} p (c_{15} + c_{21} c_{23} S_A))) \\ & + c_{23} S_A (c_{13} + c_{17} c_{24} p + c_{19} c_{23} S_A) \\ & + \sqrt{c_{23} S_A}(c_{11} + c_{24} p (c_{14} + c_{18} c_{24} p + c_{23} S_A (c_{16} + c_{20} c_{24} p + c_{22} c_{23} S_A))) \\ & - A c_{25} \left(c_{26} - \frac{S_A}{c_{27}} \right), \end{aligned} \tag{19}$$

with $c_{(0,1,\ldots,27)}$ being constants and A the saturation fraction of dissolved air in seawater. The major advantage of using the linearized equation (16) is an easy analytical solution of the 'three equation formulation' (Appendix A), whereas using (19) requires a numerical root finding algorithm as well as incorporation of a dataset for the absolute salinity anomaly δS_A (Appendix B). A direct comparison of (19) and (16) shows that the linear approach deviates at most by roughly a tenth of a centigrade for high pressures and low salinities in a typical ice shelf cavern setup, see fig. 13.

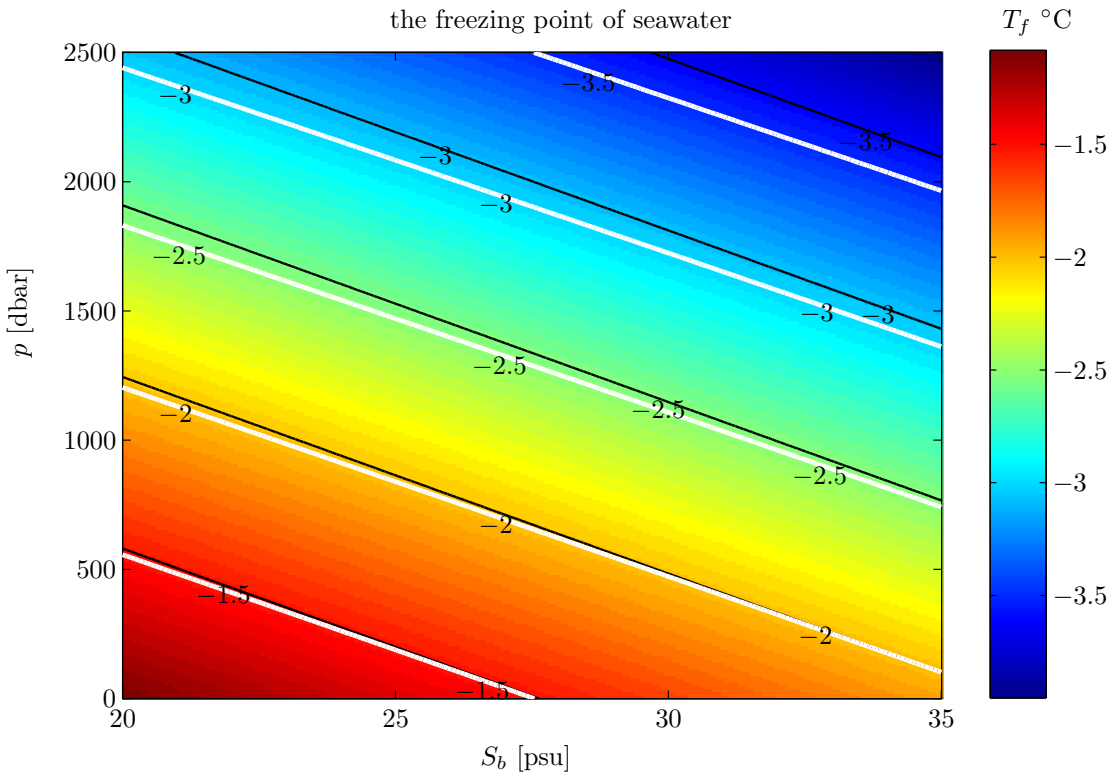

Figure 13: The potential freezing temperature of seawater in dependence on practical salinity and pressure. Black contour lines: T_f using the linearized equation (16) proposed by Jenkins et al. [22]. White contour lines and colored background: T_f using TEOS-10 [27]. The location to calculate the absolute salinity is 74.4°S and 103°W, i.e. near Pine Island ice shelf. The saturation fraction of dissolved air in sea water is set to 1. The maximum temperature difference between the two formulations is 0.1491°C at $p = 2500$ dbar and $S_b = 20$ psu.

2.5 The used 'three equation formulation'

The used parameterizations of the three equation formulation (1), (2) is written as[22]:

$$\overbrace{\rho_w c_w u_* \Gamma_T (T_b - T_w)}^{(7),\,(11),\,(15)} = \overbrace{\rho_I c_I m (T_I - T_b)}^{(6)} \overbrace{-\rho_I m L}^{(4)}, \tag{20}$$

$$\underbrace{\rho_w u_* \Gamma_S (S_b - S_w)}_{(8),\,(11),\,(15)} = \underbrace{-\rho_I m S_b}_{(5)}, \tag{21}$$

with (3) according to TEOS-10 (19) or optionally (16) as suggested by Jenkins et al.[22]. The choice of parameterization for the turbulent fluxes $\phi_B^{T,S}$ according to Jenkins et al.[22] was made, owing to ease of implementation, derivation from actual measurements and reduction of unknown parameters compared to the parameterization of Holland and Jenkins[9], while retaining dependence on the friction velocity, which the parameterization of Hellmer and Olbers[7] lacks. The heat flux through the ice shelf ϕ_I^T is parameterized according to Nøst and Foldvik[33], because competing parameterizations include unknown variables such as ice shelf thickness D, vertical ice shelf velocity ω_I and variables that are only assumed constant, i.e. the heat diffusion coefficient of ice κ_I is chosen for $T_I = -20°C$, while borehole drilling show a nonuniform temperature distribution, especially near the base, see fig. 10.
With these equations, the melting rate can be calculated as:

$$m = \rho_w u_* \Gamma_S \frac{(S_b - S_w)}{\rho_I S_b}. \tag{22}$$

The derivation is written in detail in Appendix A and B, depending on the choice of freezing point calculation. The friction velocity u_* is parameterized as in (15), with the surface roughness length z_0 being main parameter used for tuning. Fig. 14 displays melting rates for varying conditions of S_w, T_w and p. The melting rate is directly proportional to the friction velocity and the square root of the drag coefficient, hence there are no separate plots for varying u_* and C_d.

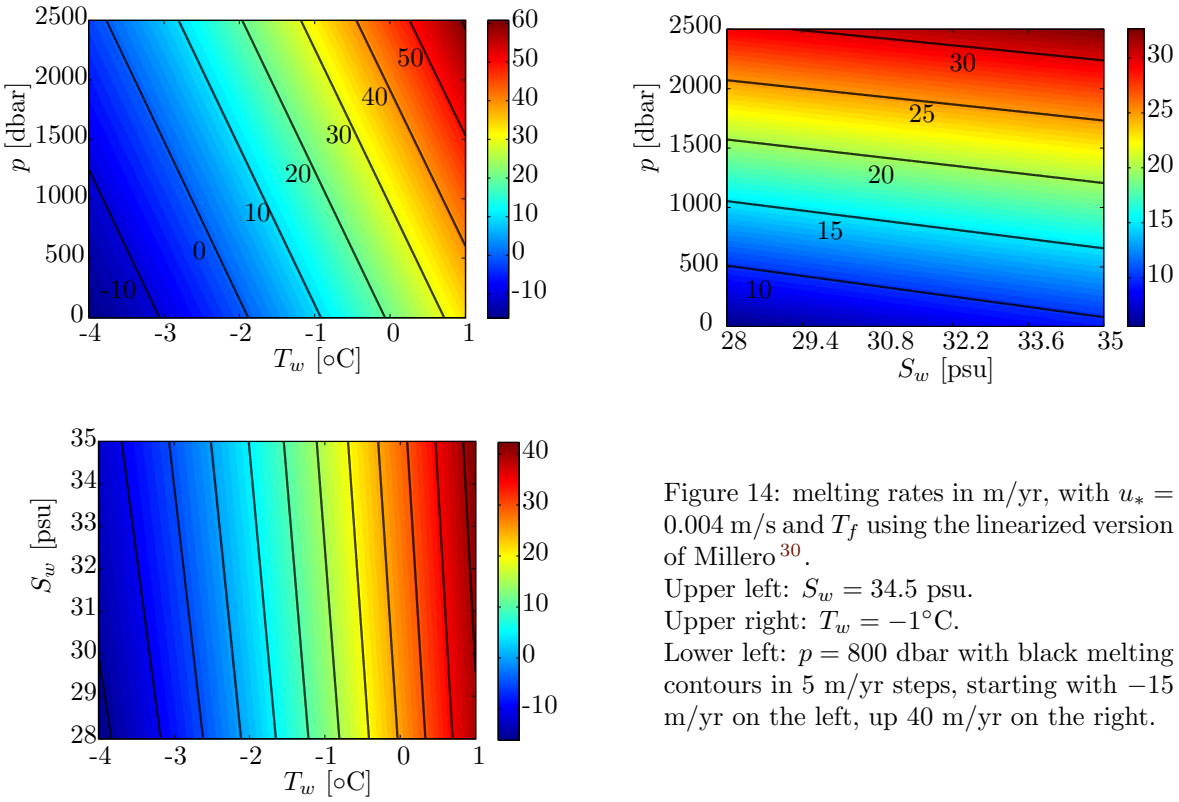

Figure 14: melting rates in m/yr, with $u_* = 0.004$ m/s and T_f using the linearized version of Millero [30].
Upper left: $S_w = 34.5$ psu.
Upper right: $T_w = -1°$C.
Lower left: $p = 800$ dbar with black melting contours in 5 m/yr steps, starting with -15 m/yr on the left, up 40 m/yr on the right.

2.6 Inconsistencies in the parameterization

Attention is required when modeling the heat and salt fluxes $\phi_B^{T,S}$, in particular the choice of the vertical resolution of the grid at the ice shelf base. For resolutions capable of resolving the interfacial sublayer, Jenkins et al. [22] cautions against the usage of the nearest vertical grid-points for determining S_w, T_w and especially the velocity U. On the one hand Jenkins et al. [22] used measurements from the surface layer to obtain $\Gamma_{T,S}$; furthermore, turbulence is suppressed closer to the ice-ocean interface, i.e. the turbulent exchange coefficient ratio R will shift towards a molecular exchange coefficient ratio of $R_m \approx 200$ for cold seawater, thus decreasing the melting rate, see fig. 15. Γ_S is calculated using (9):

$$\Gamma_S = \frac{1}{R}\Gamma_T.$$

On the other hand McPhee [29] stresses that grid-points too far from the wall require a different parameterization of the drag coefficient, due to buoyancy production from ice shelf melting or freezing in the upper surface layer. Jenkins et al. [22] took measurements of boundary layer water properties from 2 to 25 meters below the RON ice shelf; however, using temperatures and salinities within this range might not be appropriate, because surface layer thickness is variable. The heat and salt transfer through the interfacial sublayer exhibits marginal susceptibility to quantities found beyond the upper surface layer [22,41], therefore increasing the difficulty to find an appropriate distance to the ice shelf draft and an accompanying vertical resolution of the grid. Both parameterizations of Holland and Jenkins [9] and Jenkins et al. [22] use constant drag coefficients, i.e. they lack detailed parameterizations of the velocity profile near the ice shelf and using the 'law of the wall' is mainly chosen to keep consistency with the existing parameterization of the bottom friction velocity in GETM and GOTM.

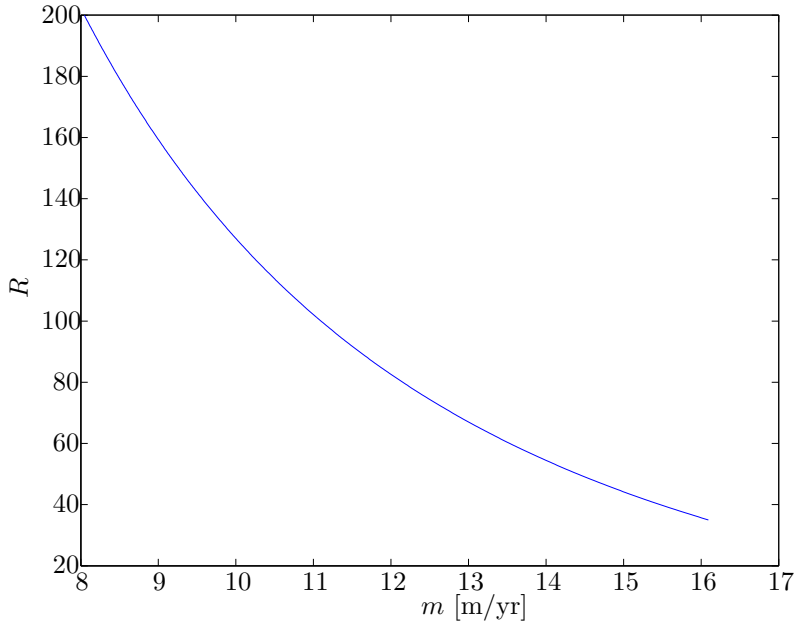

Figure 15: The melting rate according to (22) for varying exchange coefficient ratios[29] ranging from typical turbulent values from 33 to 77, up to molecular ratios of 200 for cold seawater. Other variables, which are needed to calculate m are set to the following values: $u_* = 0.004$ m/s, $T_w = -1°\mathrm{C}$, $S_w = 34.5$ psu, $\Gamma_T = 0.011$ and $p = 800$ dbar.

3 One-dimensional gravity current parameterization

With the parameterization of the heat (20) and salt fluxes (21) it becomes evident that a water mass at rest will never lead to any melting or freezing, because the turbulent exchange coefficients $\gamma_{T,S}$ depend on the friction velocity u_*, see (11). To investigate the evolution of water at the base of an ice shelf and the associated melting rate, a forcing of momentum is needed. A column of water under the ice shelf is considered and subdivided into two regimes: A boundary layer of buoyant ISW above a thick passive layer of ambient sea water with homogeneous density. In accordance with the parameterization of Arneborg et al. [1] for modeling a one-dimensional bottom gravity current, the x-axis of the coordinate system is aligned with the local slope of the ice shelf Sl_{ice}, i.e. $Sl_{ice} = Sl_x = \tan(\alpha)$ and the z-axis is parallel to the local upward normal vector of the ice shelf; therefore the Coriolis parameter is a projection on the z-Axis, i.e. $f' = f\cos(\alpha)$, where α is the local angle of elevation of the ice shelf. The Reynolds Averaged shallow water equation without advection, horizontal mixing nor atmospheric or external pressure gradients can be written as:

$$\begin{aligned}\frac{\partial u}{\partial t} - f'v &= -\frac{g}{\rho_0}\int_{z_b}^{z_i}\frac{\partial p}{\partial x}dz + \frac{\partial}{\partial z}\left((\nu_t+\nu)\frac{\partial u}{\partial z}\right),\\ \frac{\partial v}{\partial t} + f'u &= -\frac{g}{\rho_0}\int_{z_b}^{z_i}\frac{\partial p}{\partial y}dz + \frac{\partial}{\partial z}\left((\nu_t+\nu)\frac{\partial v}{\partial z}\right),\end{aligned} \tag{23}$$

with z_i being the depth at the base of the ice shelf and z_b being an arbitrary depth well within the ambient water. For the purpose of this section the buoyancy is defined as

$$b = -g\frac{\rho-\rho_0}{\rho_0}, \tag{24}$$

where ρ_0 is the density of the ambient water and ρ is the density of the ISW. Considering a vertical water column with a local idealized stable stratification pattern, the isopycnals are parallel to the ice shelf base; therefore, the internal pressure gradient in (23) can be written as

$$\begin{aligned}\frac{g}{\rho_0}\int_{z_b}^{z_i}\frac{\partial p}{\partial x}dz &= \frac{g}{\rho_0}(\rho-\rho_0)Sl_x = -bSl_x\\ \frac{g}{\rho_0}\int_{z_b}^{z_i}\frac{\partial p}{\partial y}dz &= bSl_y = 0,\end{aligned} \tag{25}$$

and inserting (25) in (23) yields

$$\begin{aligned}\frac{\partial u}{\partial t} - f'v &= bSl_x + \frac{\partial}{\partial z}\left((\nu_t+\nu)\frac{\partial u}{\partial z}\right)\\ \frac{\partial v}{\partial t} + f'u &= \frac{\partial}{\partial z}\left((\nu_t+\nu)\frac{\partial v}{\partial z}\right),\end{aligned} \tag{26}$$

thus the forcing of momentum is found in the first term on the right hand side of the upper equation of (26) with the requirement of an initial buoyancy profile and slope unequal 0. Vertical integration of (26), as done in detail in Appendix C, leads to the following set of equations, that can be used to find

a set of parameters to arrive at a stable regime:

$$Fr = \sqrt{\frac{\tan(\alpha)K}{C_d\sqrt{K^2+1}}}, \tag{27}$$

$$K = \tan(\beta) = -\frac{|\mathbf{U}|}{Hf'}C_d, \tag{28}$$

$$\frac{G'}{H} = \left(\frac{f'}{C_d}\frac{K}{Fr}\right)^2, \tag{29}$$

where Fr is the Froude Number, K the Ekman number, C_d the drag coefficient, β the deflection angle of the mean flow U due to the Coriolis force, G' the reduced gravity acceleration and the H the layer depth. For $|K| \gg 1$ (e.g. $f' \to 0$ in (28)) the Froude number (27) converges to

$$Fr = \sqrt{\frac{\tan(\alpha)}{C_d}} = \sqrt{\frac{U^2}{G'H}}, \tag{30}$$

i.e. the flow due to the slope of the ice shelf is balanced by the friction and the regime will become unstable if the slope approaches or surpasses the drag coefficient.

3.1 Parameter Ranges

Using Equations (27) and (30), a preliminary narrowing of the parameters f, C_d and Sl_x is helpful in order to find stable regimes for G' and U. Lu et al.[26] compiled a list of ice-ocean drag coefficient measurements for a variety of different sea ice forms with a range of $0.13 \cdot 10^{-3} \leq C_d \leq 22.08 \cdot 10^{-3}$, although the majority of measurements was in a range of $1 \cdot 10^{-3} \leq C_d \leq 8 \cdot 10^{-3}$. With Latitudes ranging from $84.3°$S near the grounding line of ROS up to $67.5°$S near the grounding line of LAR, the Coriolis parameter has a range of $-1,45 \cdot 10^{-4}\text{s}^{-1} \leq f \leq -1,35 \cdot 10^{-4}\text{s}^{-1}$. The slope is usually steep near the grounding line and diminishes for the remaining ice shelf, e.g. the draft of PIIS changes 400 m within the first 20 km distance to the grounding line and 100 m for the adjacent 40 km, see fig. 5. While this picture differs between the different ice shelves, a broad range of $0.0025 \leq Sl_{\text{ice}} \leq 0.02$ is viable as a preliminary restriction for the slope. These ranges are listed in table 2 as a quick reference. Equation (27) can be solved for K:

$$K = \pm\frac{Fr^2}{\tan^2(\alpha){C_d}^{-2} - Fr^4}. \tag{31}$$

Inserting (31) into (29) leads to

$$\frac{G'}{H} = \left(\frac{f'Fr\,C_d}{\tan^2(\alpha) - Fr^4{C_d}^2}\right)^2, \tag{32}$$

i.e. the ratio of G' to H is dependent on constrained variables, if Fr is set to a certain type of regime. Implicitly (32) is still dependent on the deflection angle β, because Fr depends on K, as shown in fig. 16. Typically $Fr \geq 1$ corresponds to an unstable regime; however, Fr can be chosen to correspond to a stable regime ($Fr = 0.8$) or a marginal stable regime ($Fr = 1$). Equation (32) has a singularity for $\tan(\alpha) = Fr^2C_d$, which corresponds to regions where there is no solution for the chosen Froude number, e.g. $Fr = 1$ leads to a singularity in case of $\tan(\alpha) = C_d$, which corresponds to (30). For $\tan(\alpha) > Fr^2C_d$ equation (32) produces non-physical results. Approaching the singularity, $G'H^{-1}$ increases rapidly which is possible if either H decreases or G' increases. In a one dimensional case without advection, H can only decrease in case of negative entrainment, a process not observed in

nature, because entrainment produces entropy. G' can only increase in case of buoyant melt water production in the boundary layer; however, high values for G' imply high velocities, hence increased melting rates. The occurrence of strong salinity and heat fluxes in the surface layer, leads to creation of a separate sublayer within the ISW with melt water at or near the freezing point and the lower part of the ISW loosing density gradients due to entrainment with the ambient sea water. In case of advection H can decrease by advecting parts of the buoyant melt water slope upwards; additionally, a separate sublayer will be advected at a different pace than the ISW. The Froude Number within the parameter ranges is displayed in fig. 16. There are no solutions with $Fr \leq 1$, for some ratios of $\tan(\alpha)\, {C_d}^{-1}$. Fig. 18 and fig. 17 show the solutions of (32), for varying C_d and Fr. The Coriolis parameter is set to $f' = 1.4 \cdot 10^{-4}$ and there are no plots for varying f' because (32) is explicitly directly proportional to ${f'}^2$. There is still the implicit dependency, because Fr depends on K and is thus affected by f'. The parametrization predicts either unstable regimes near grounding lines (having the steepest slope of the ice shelf) or stable regimes with a thin layer (small H) of melt water (high G') that is quickly advected slope upwards.

Table 2: Parameter Ranges

Variable Range	Exponent	Unit
$1 \leq C_d \leq 8$	10^{-3}	
$-1,45 \leq f \leq -1,35$	10^{-4}	s^{-1}
$0.25 \leq Sl_{\mathsf{ice}} \leq 2$	10^{-2}	

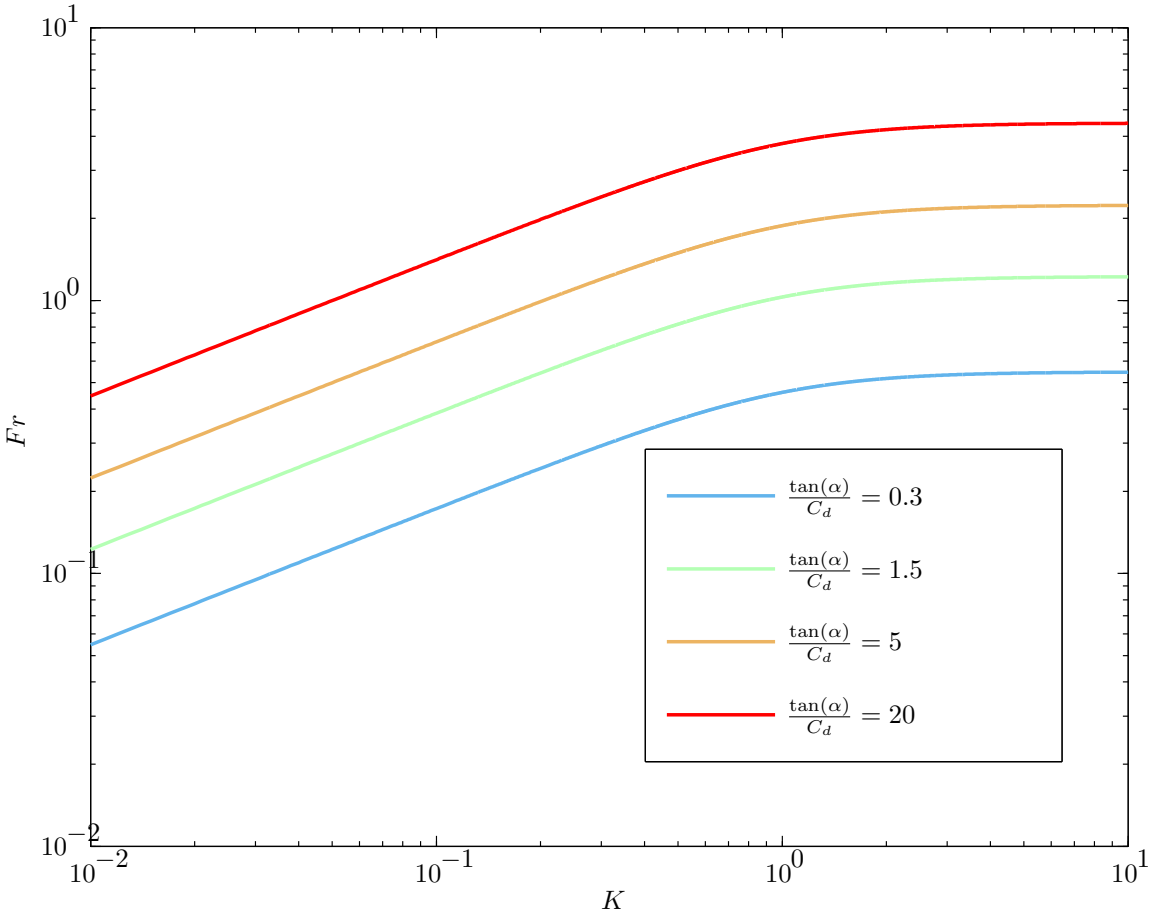

Figure 16: The Froude Number according to (27), for selected $\frac{\tan(\alpha)}{C_d}$ with ranges according to table 2. For greater slopes no $Fr \leq 1$ can be found.

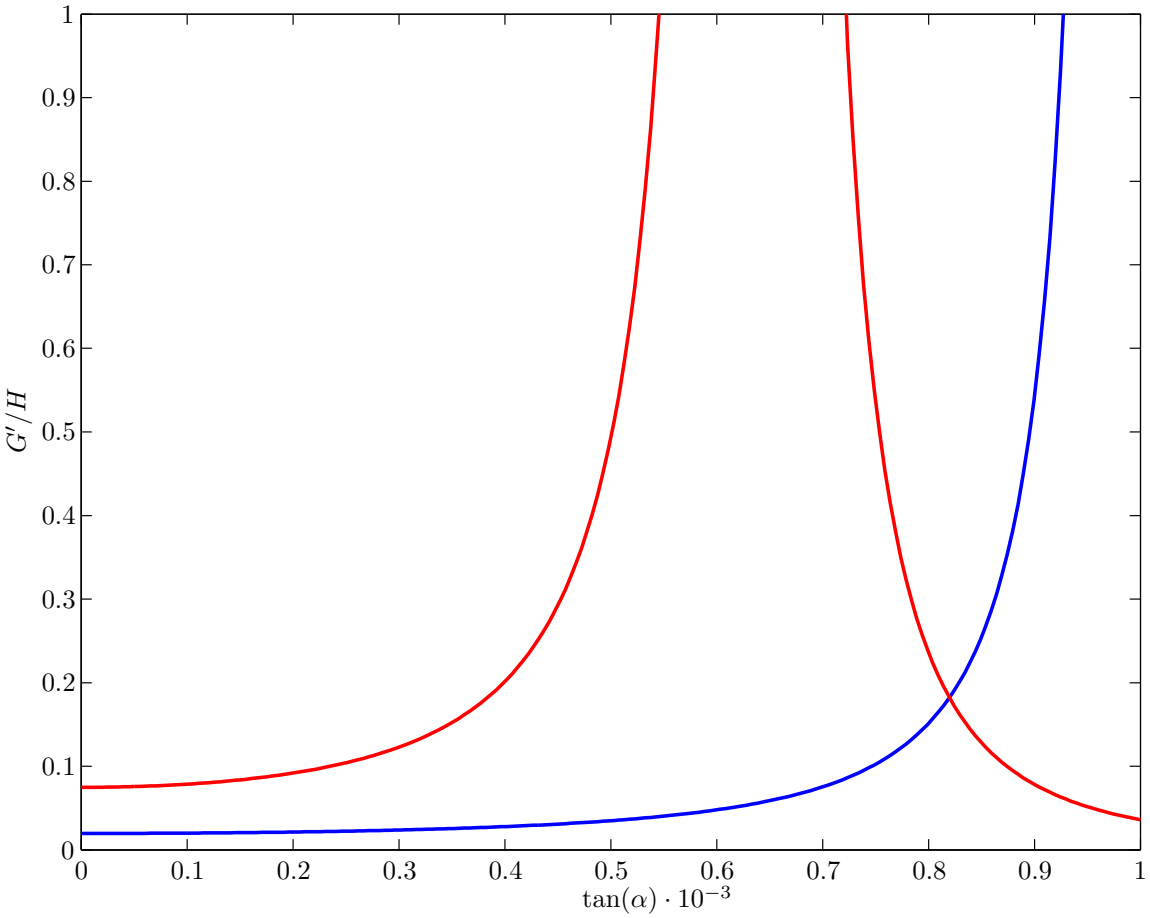

Figure 17: $G'H^{-1}$ according to (32) with $C_d = 1 \cdot 10^{-3}$. The red curve corresponds to $Fr = 0.8$ which moves the singularity in (32) near smaller slopes. The values on the right side of the singularity are non-physical solutions of $G'H^{-1}$. The blue curve corresponds to $Fr = 1$; therefore, the singularity occurs exactly at $Fr\, {C_d}^{-1} = 1$. Solutions for stable regimes ($Fr < 1$) allow for greater values of $G'H^{-1}$.

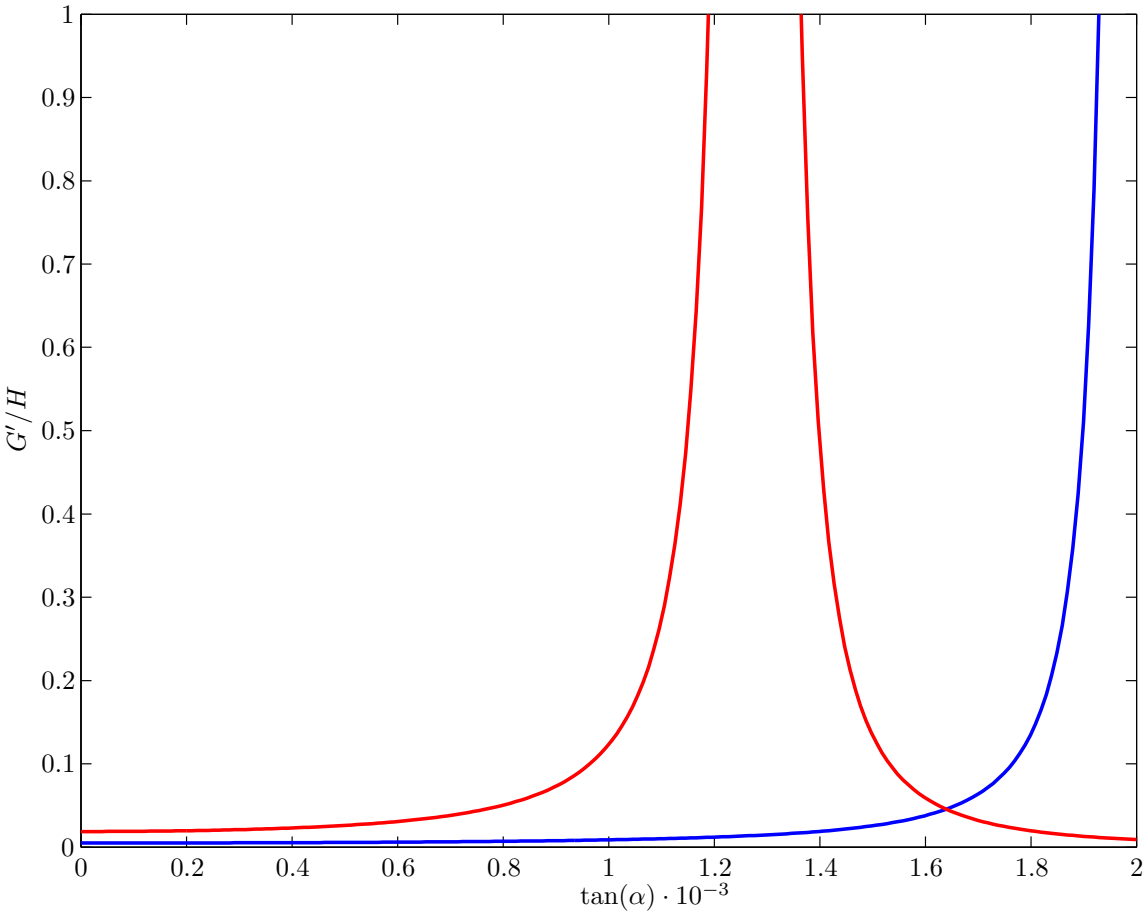

Figure 18: A similar figure to fig. 17, with $C_d = 2 \cdot 10^{-3}$. The singularity in the solutions of (32) move to greater slopes accordingly (note the different scale of the x-axis). The red curve uses $Fr = 0.8$ and the blue curve $Fr = 1$. Compared to smaller drag coefficients, $G'\,H^{-1}$ is smaller for small slopes, i.e. the ISW plume can be thicker or have a lesser density difference with the ambient sea water if C_d is increased.

4 Results and Discussion

4.1 Model runs and setups

The model is setup for different runs, integrating until a steady state is found, which usually takes two weeks to a month of simulation time. The model runs are extend by at least two months of simulation time, in order to verify the steady state. The slice model option ($j_{max} = 4$) is used, i.e. all y-velocity-components are zero ($v(i, j, k) = 0$) and the domain is enclosed by land grid-points. All runs share a uniform distribution of the initialization fields $S_{init} = 35$ psu and $T_{init} = 0.5°$C. The initial forcing is done by modifying the first nine vertical columns of the initial temperature field and increasing the temperature by $0.2°$C, i.e.

$$T_{init}(i, j, k) = 0.7°\text{C},$$

with ($i = 0 : 8$), see fig. 20. This produces an instability near the grounding line and the warmer water is advected following the slope of the ice shelf draft; in turn, this will produce friction velocities at the ice shelf base leading to creation of salt and temperature fluxes. The nudging fields are identical to the tracer fields, i.e. ($T_{nudge} = T_{init}$) and ($S_{nudge} = S_{init}$) and the relaxation-time-fields are set to

$$T, S_{nudge}(i, j, k) = [0, \ldots 0,\ 0.125,\ 0.1429,\ 0.1667,\ 0.2,\ 0.25,\ 0.5,\ 1],$$

with ($i = 0 : i_{max}$), i.e. with values greater zero for the last eight vertical columns. This means the strongest nudging is experienced at the end of domain, where the tracer fields for salinity and temperature have always the same value as the nudging, hence the the initial fields. The used implemented nudging routine is described in Appendix D.2 and does not use implicit nudging of the tracer fields within the advection and diffusion routines; therefore, the relaxation fields are not comparable to relaxation times. A proper implicit nudging is proposed in Appendix D.2, but was not used due to ease of use of the current implementation.

Four different runs were made:

- *R1* A constant surface slope with a low resolution of the surface boundary layer.
- *R2* Same as run 1, with a high resolution of the surface boundary layer, doubling the vertical grid points and employing heavy zooming towards the surface
- *R3* An idealized surface slope of an ice shelf with a small surface roughness length and the same vertical resolution options used by run 2.
- *R4* Same as run 3, with an increased order of magnitude of the surface roughness length.

The bathymetry was set to a constant depth of 1000 m and the length of the cavern was set to 100 km. The vertical grid uses sigma layers, with [*R1*] using 40 layers and weak zooming at surface and bottom. [*R2*], [*R3*] and [*R4*] use 80 layers with strong zooming at the surface and no zooming at the bottom. The horizontal grid uses constant steps of $d_x = d_y = 1000$ m for all runs. The cavern geometries are displayed in fig. 19. [*R1*] was computed with a time step of 2 seconds all other runs used 0.5 seconds. The entire grid of [*R2*], [*R3*] and [*R4*] can not be displayed, while still providing readable information due to the strong surface zooming and the high amount of layers. A section of the [R2] grid is displayed in fig. 21. Options for the ice shelf module are described in table 5 and the following choices were made: Melting rate, heat and salt flux are calculated using TEOS-10, employing a zero finding algorithm as described by Zhang[46], with a maximum iteration count of 50 and a convergence criterion of $1 \cdot 10^{-6}$. The saturation fraction of dissolved air in seawater is set to 1 and δS_A is calculated with the TEOS-10 functions and data set, using the coordinates $-74.4°$S and $103°$W, i.e. near PIIS.

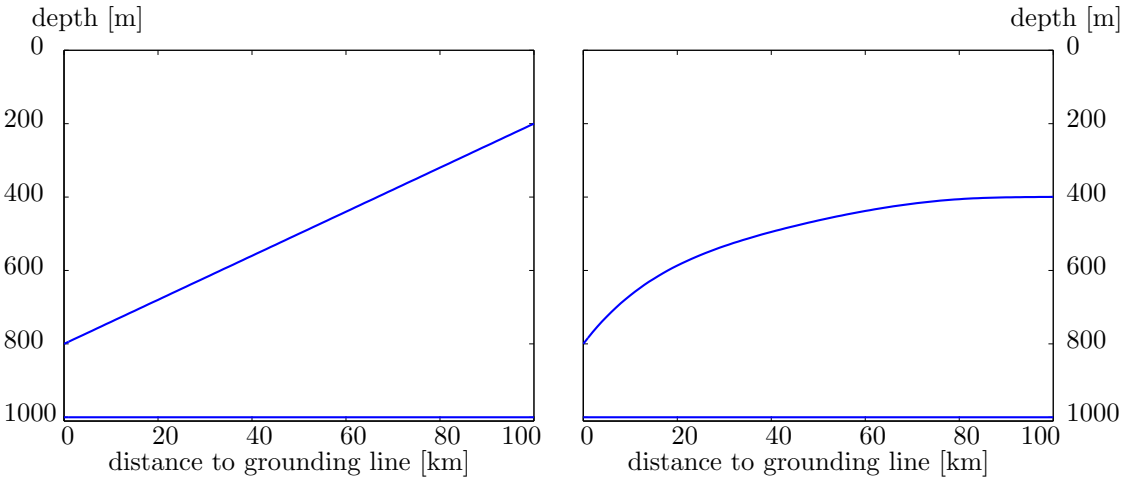

Figure 19: The bathymetry and elevation (ice shelf draft) of the runs [R1], [R2] on the left and [R3], [R4] on the right. The displayed data is taken from GETM netCDF output.

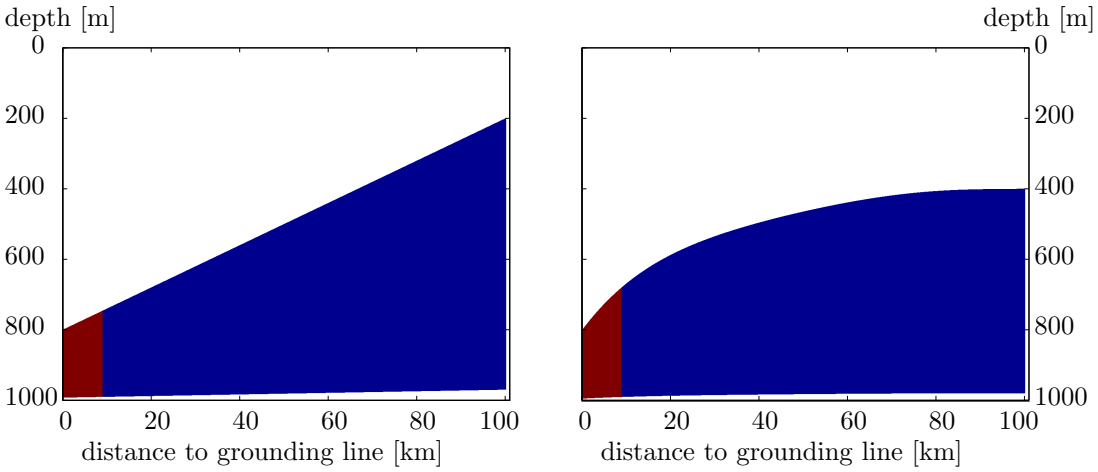

Figure 20: T_{init} after import into GETM, for the runs [R1], [R2] on the left and [R3], [R4] on the right. Red areas correspond to a temperature of 0.7°C and blue areas correspond to 0.5°C.

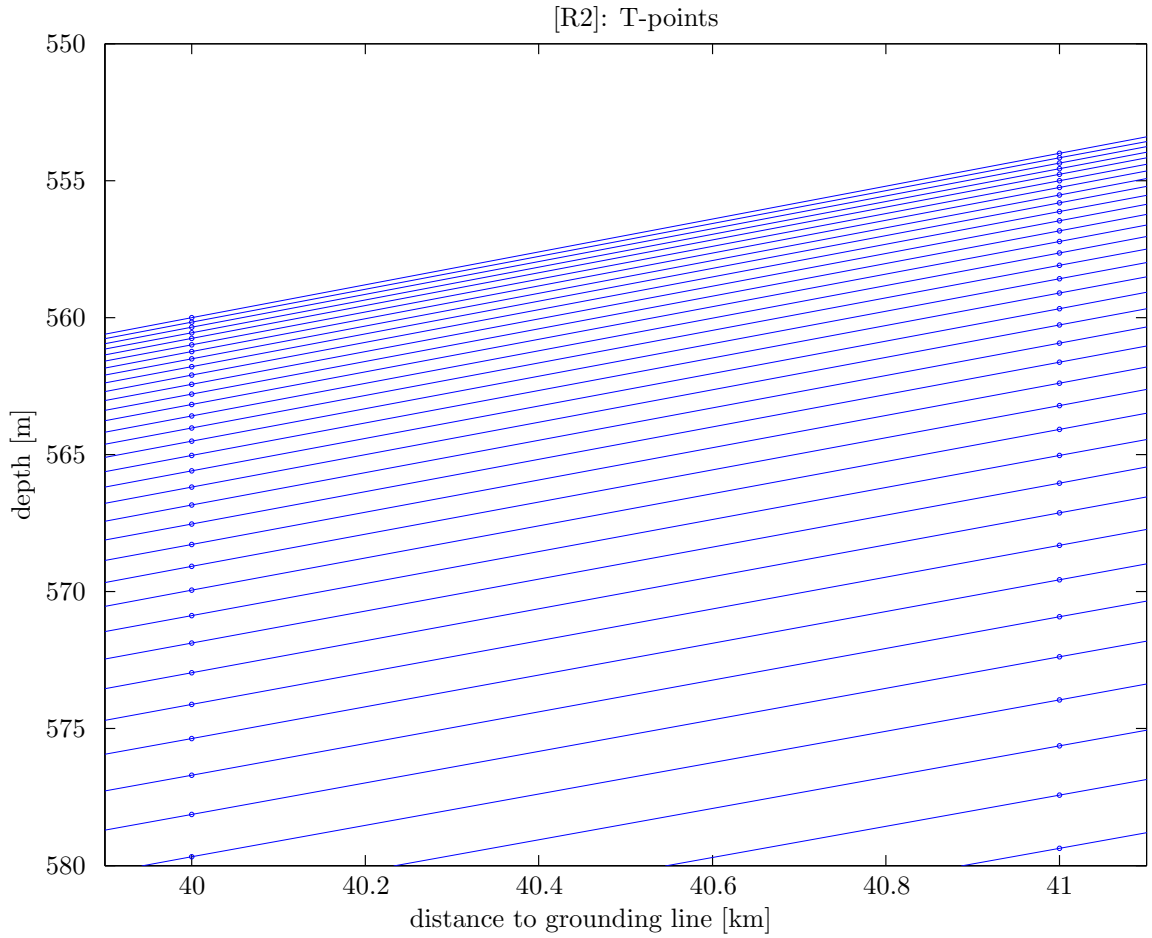

Figure 21: Detail of the [R2] grid near the surface for the velocity-points (dots). The top left grid point has a vertical distance to the ice shelf draft of 0.17 m and the ratio of drag coefficient to the slope is ($C_d/Sl_x \approx 1.42$). [R3] and [R4] have a similar grid resolution, due to comparable setups.

4.2 Model results

Plot-titles which display the model time step and calculated time, use an arbitrary starting point set to 1. January 2000. Calculated values of any variable located at a distance of 80 or more kilometers to the grounding line can be safely dismissed, due to the chosen nudging method. For specific depths of tracer variables given in the text, the interpolation on the layer heights is regarded, for vertical profile plots it is ignored. Due to the vertical axis resolution this error will not be noticeable in the first place. The location of the vertical grid at a distance of 40 kilometers to the grounding line is referenced as d1 and the location with 20 kilometers distance to the grounding line is named d2. Comparisons of vertical profiles can be made between all runs, because the horizontal resolution is unchanged.

4.2.1 Influence of vertical resolution: comparing [R1] to [R2]

Fig. 22 shows [*R2*] during it's forcing period. Clearly shown is the warm melting plume flowing along the ice shelf draft. Due to the induced velocities at the ice shelf base, a thin layer of melt water is created. High density gradients between the melt water and rest of the water body increase advection speed and the melt water will rise faster along the ice shelf base than the initial warm water plume that forces the model. Fig. 23 displays [*R2*] and fig. 24 shows [*R1*] at a later time in their respective steady states. The temperature field of [*R2*] can not be displayed, because notable temperature differences are only found in the first layer and the rendering routines fail to display this. In the steady state, the initial warm water plume has been absorbed due to nudging and ambient cavern water has taken it's place. The melt water plume sustains itself due to advection velocities and constant replacement of advected melt water with either melt water from further downslope or ambient cavern water. A comparison between vertical profiles of [*R1*] and [*R2*] at d1 is shown in fig. 25 for the density, in fig. 26 for the turbulent kinetic energy and in fig. 27 for the x-components of the velocity (u). Fig. 28 shows the complete vertical profile of the x- and z-components of the velocity at d1 for [*R2*]. The z-component of the velocity (w) shows high positive values near the grounding line with $2.42 \cdot 10^{-4} < \mathrm{w} < 3.99 \cdot 10^{-4}$. Leaving the grounding line behind, w stays positive but looses an order of magnitude inside the ambient water mass. The relation of u/w in top layer is 1, if the resolution ratio of the cavern geometry is accounted for, i.e. the velocities at the base of the ice are parallel to the slope. The basic principal of a convection cell is therefore simulated; however, there are strong oscillations in the velocity fields near the calving line, which are artifacts from the nudging of temperature and salinity fields. Comparison of [*R1*] and [*R2*] shows significant differences in the melting rates, especially near the grounding line. It is not evident what causes this implicitly. Explicitly the melting rate is dependent on the friction velocity, salinity and temperature of the top layer and there might be underlying processes that cause a difference in these water mass properties. An in-depth analysis showing what routines precisely contribute to these differences would require extensive debugging, which goes beyond the scope of this thesis. The obvious reason that a finer resolution near the surface leads to a more precise calculation of those properties should not be taken at face value. As discussed in 2.6, the values for $\Gamma_{T,S}$ could be off, in case of a vertical grid with high resolution, overestimating the melting rate. Different melt rates near the grounding line affect processes further upslope and must not be ignored and the differences in the melting rates near the grounding line are the most striking results of the comparison of [*R1*] and [*R2*]. A concerning property of [*R2*] are increasing melting rates further upslope. The melt rate depends on friction velocity and suppression of the freezing point. The velocity of [*R2*] increases further upslope, e.g. u of the closest layer to the ice shelf draft increases from 0.0356 [m/s] at d2 to 0.0548 [m/s] at d1; therefore, it can be argued that freezing point depression contributes less to the melting rate than the friction velocity, which is calculated from u(k = kmax). Moving towards the calving line, the melt water plume increases in depth, i.e. layers that are less affected by surface friction are able to advect faster, which in turn increases the surface friction velocity, due to friction between the layers and the velocity profiles of [*R2*] show maxima within the melt water plume.

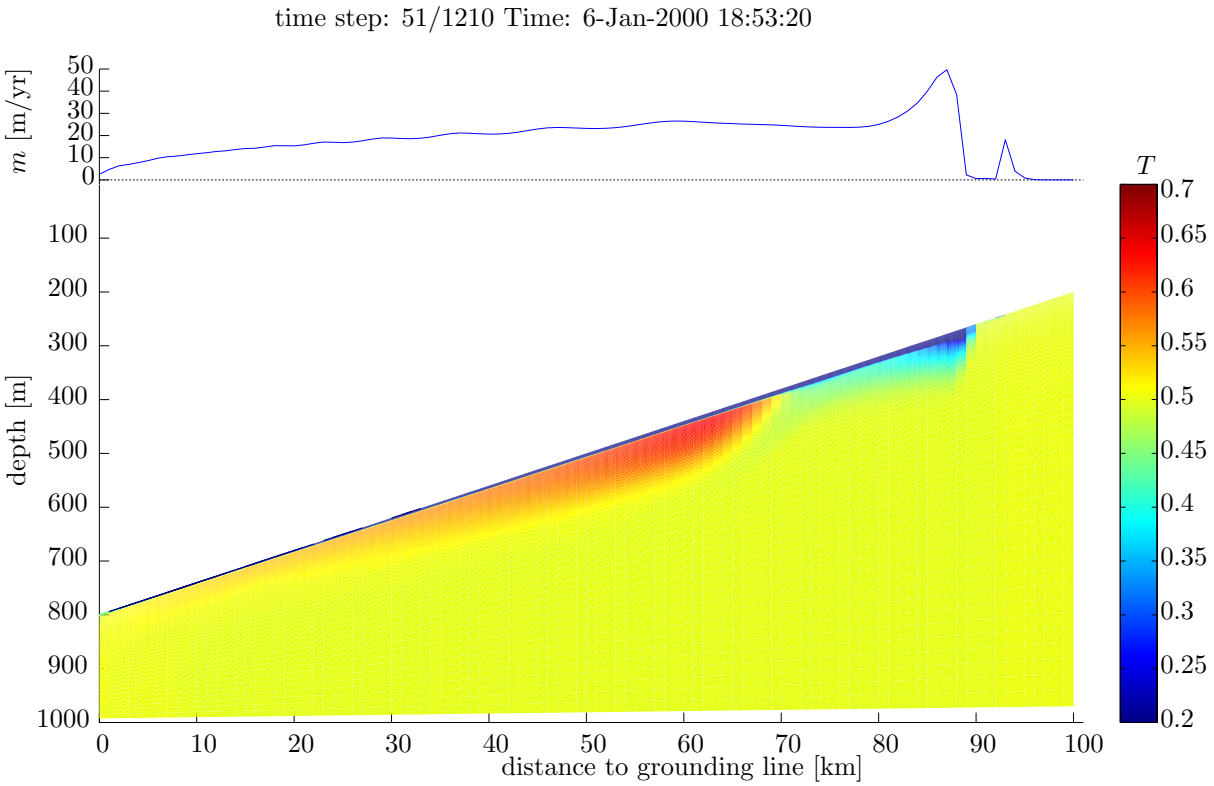

Figure 22: [R2] during it's forcing period. The lower part of the plot shows the temperature field T and the upper plot shows the melting rate m. The title displays the model time step and calculated time, with an arbitrary starting point set to 1. January 2000.

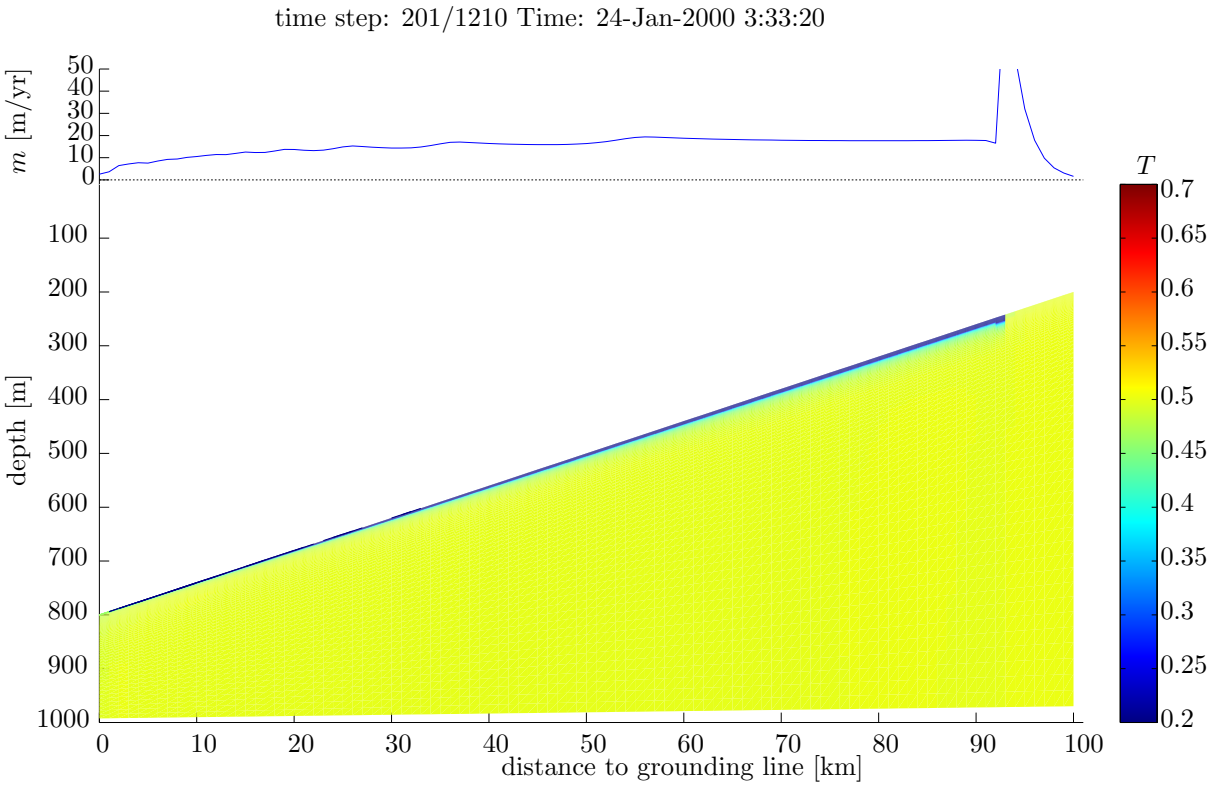

Figure 23: [R2] in it's steady state. Temperatures lower than 0.2°C are displayed in the same color as 0.2°C

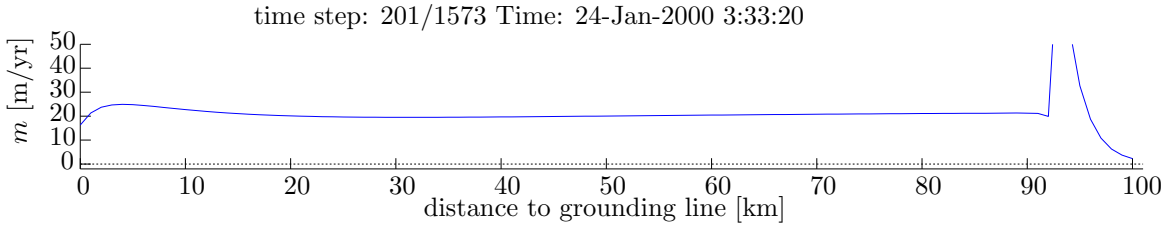

Figure 24: The melting rate of [R1] in it's steady state. There are notable differences in the melting rate, compared to the steady state of [R2], especially near the grounding line.

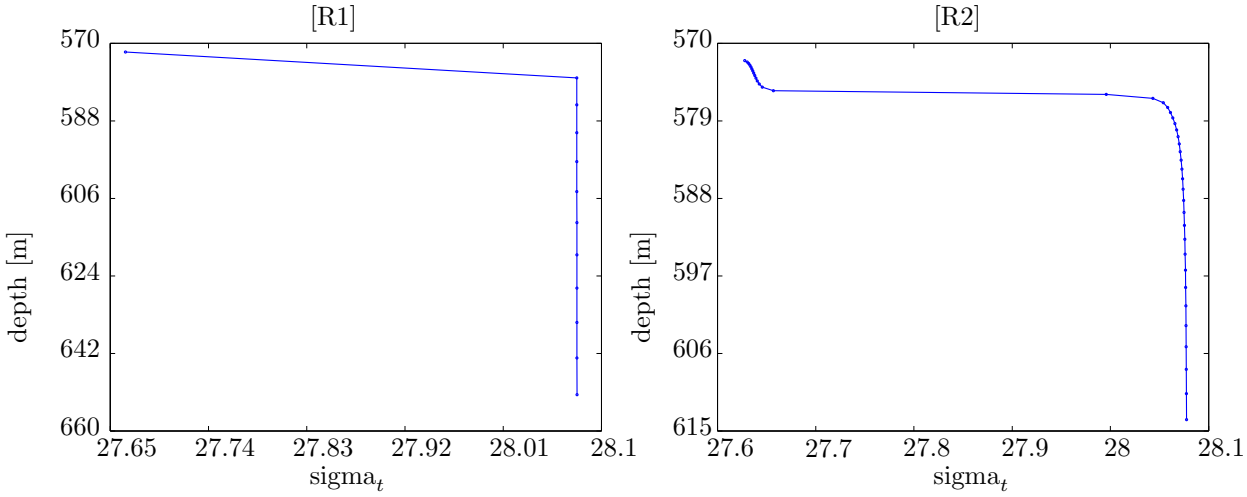

Figure 25: Comparison between [R1] and [R2], showing sigma$_t$ (with sigma$_t$ $= \rho - 1000$) of the upper layers at d1. [R1] shows a density gradient (Δsigma$_t > 0.3$) in a depth of 3.005 meters below the ice shelf draft and [R2] shows a similar gradient at 3.7 meters.

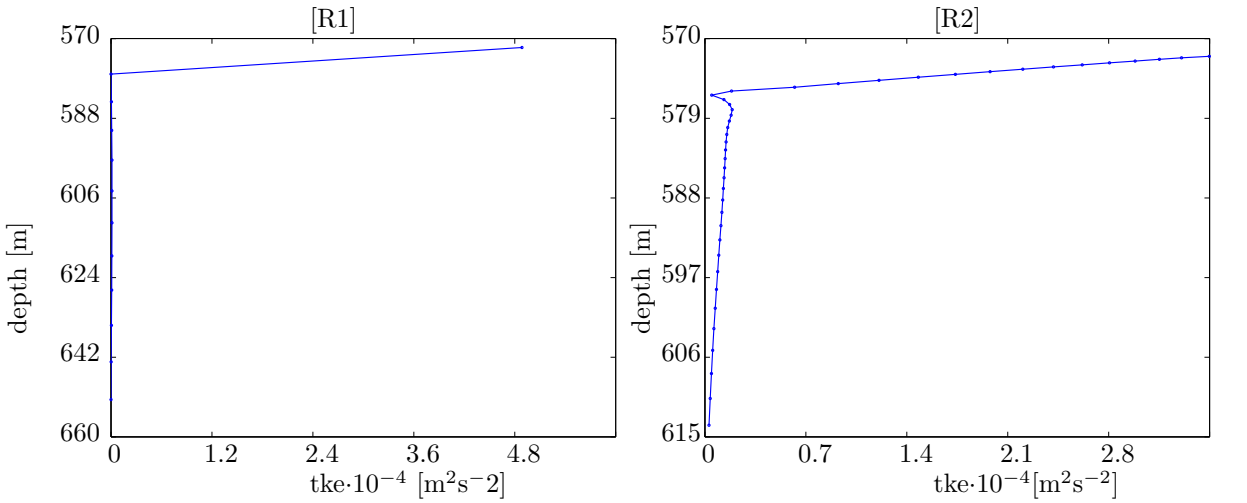

Figure 26: Comparison between [R1] and [R2], showing the turbulent kinetic energy [m^2 s^{-2}] of the upper layers at d1. [R2] shows suppression of turbulence at the melt water plume depth due to stratification, and turbulence occurs mostly within the plume, while being negligible in the ambient water.

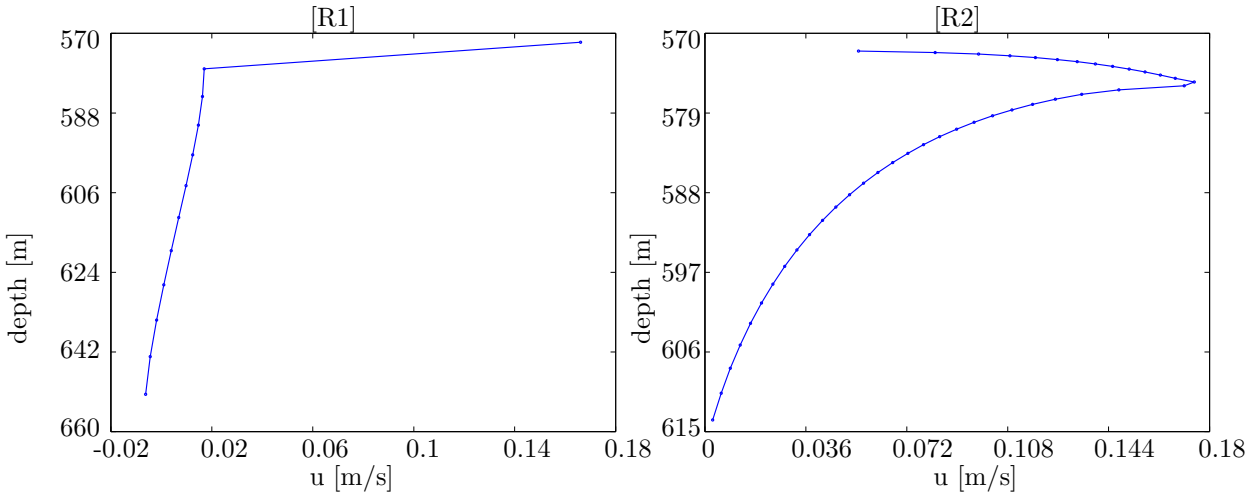

Figure 27: Comparison between [R1] and [R2], showing the x-component of the velocity [m s^{-1}] of the upper layers at d1.

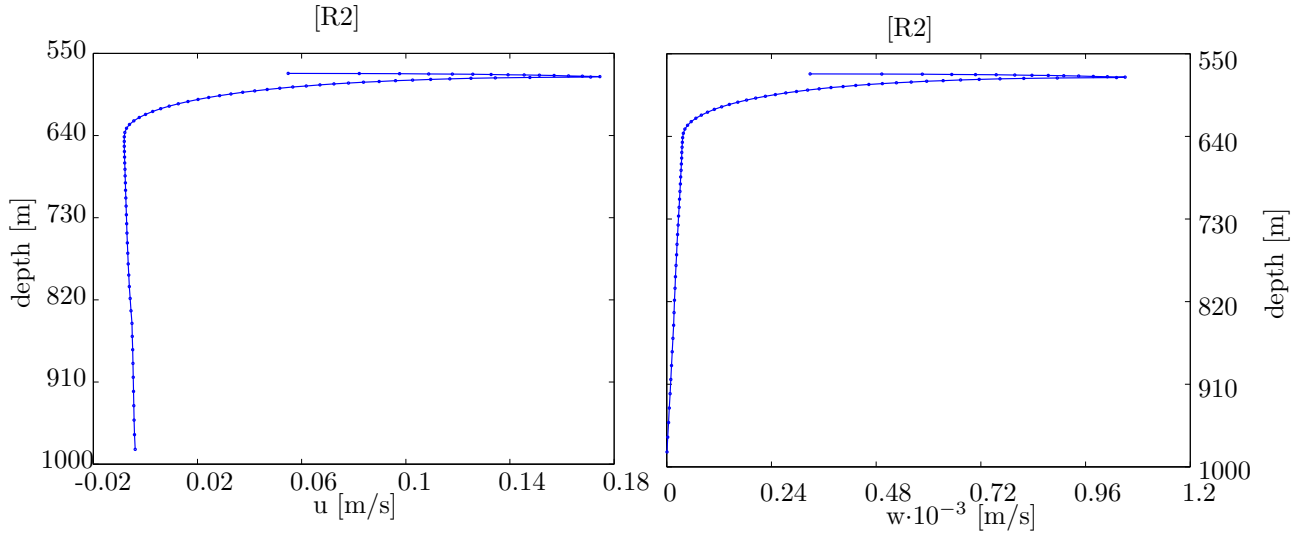

Figure 28: The complete vertical profiles for [R2] of the velocities u and w [m s^{-1}] at d1. The vertically integrated u-velocity is zero (u_advection from GETM output) and fulfills the rigid lid boundary condition (52).

4.2.2 Influence of surface roughness: comparing [R3] to [R4]

The general characteristics of the convection cell within the cavern of [*R3*] and [*R4*] are very similar to the one described for [*R2*] in 4.2.1. In contrast to [*R2*] the melting rate distribution represents an actual ice pump, i.e. there are high melting rates near the grounding line to low melting rates approaching the calving line. Such a melting rate distribution therefore pumps ice away from the grounding line and is responsible for the typical cavern geometry with a deep grounding line with steep slopes that decrease as the calving line is approached, as described in 1.1. The difference between [*R3*] and [*R4*] is a change in surface roughness length with $z_0 = 0.001$ for [*R3*] and $z_0 = 0.01$ for [*R4*]. Increasing the surface lengths strongly decreases top layer u velocities. For d1 the ratio of top layer u velocities is

$$\frac{u([R3], d1, k = kmax)}{u([R4], d1, k = kmax)} \approx 2.9,$$

and for d2 the ratio is

$$\frac{u([R3], d2, k = kmax)}{u([R4], d2, k = kmax)} \approx 3,$$

see fig. 32. [*R3*] and [*R4*] use the same grid, hence the surface friction velocity ratio is the same. Turbulence is increased for greater surface roughnesses within the melt water plume, but still suppressed at the plume depth, see fig. 31. Melt water layer depth is increased due to increased entrainment of ambient cavern water, see fig. 33. Density differences between [*R3*] and [*R4*] in the top layer are negligible, see fig. 30. The melting rates are significantly greater in [*R4*] especially near the grounding line, see fig. 29. The increased melting rates can be explained by increased entrainment of ambient cavern water in [*R4*]. Because densities of the melt water plumes show little differences, the increased entrainment forces greater buoyancy fluxes, i.e. the melt water plume shows greater sensibility to the ambient water masses for increased surface roughness, especially closer to the grounding line (compare $(\nu_h \cdot N^2)$ of [*R4*] at d1 with d2 in fig. 33). For a distance of 4 kilometers to the grounding line (named d3) [*R3*] has a drag coefficient of $C_d = 0.011$ for the surface friction velocity (i.e. half a vertical grid point under the ice shelf) and a slope of $Sl_x = 0.0148$, i.e. $Fr > 1$. This increases entrainment slightly. Density gradients are only slightly less pronounced compared to stable regimes further upslope at d2 or d1; in comparison, the layer height decreases rapidly in the vicinity to the grounding line, e.g. $H(d1) \approx 7.74$ m, $H(d2) \approx 4.54$ m and $H(d3) \approx 1.12$ m, i.e. melt water advection that reduces the melt water layer height is the main driver of keeping the regime stable, as suspected in 3.1 and accompanied by slightly greater entrainment. Without advection the regime will produce increased entrainment rates and a thickening of the melt water plume would occur.

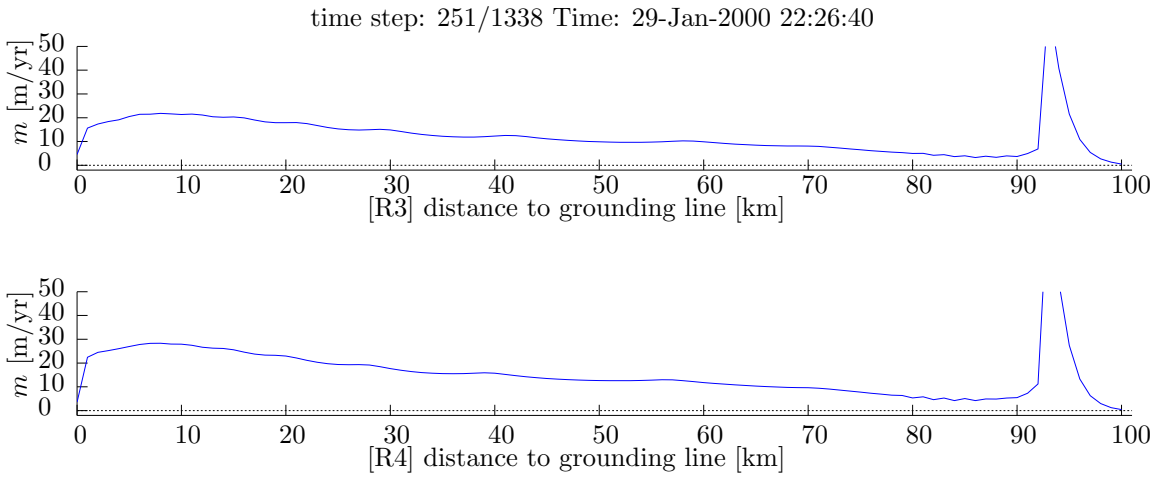

Figure 29: Comparison of the melting rates of [R3] and [R4] for the same time steps, both in stable states.

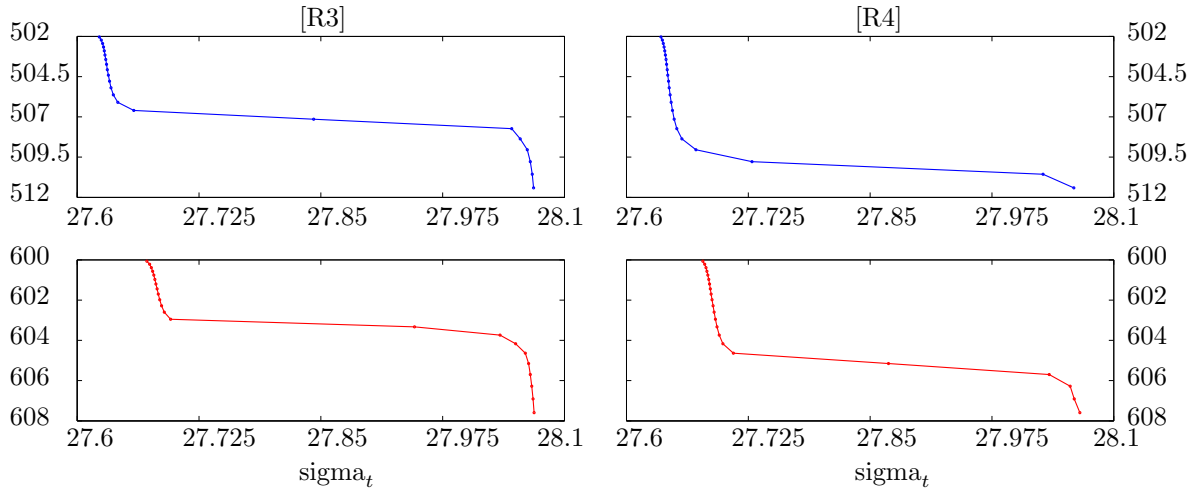

Figure 30: Vertical profile of the upper layers of sigma$_t$ at d1 (blue curve) and d2 (red curve) for [R3] on the left and [R4] on the right. Z-axises correspond to depth in meters. The z-axis labels are omitted in the plot to allow for higher resolution of the figure.

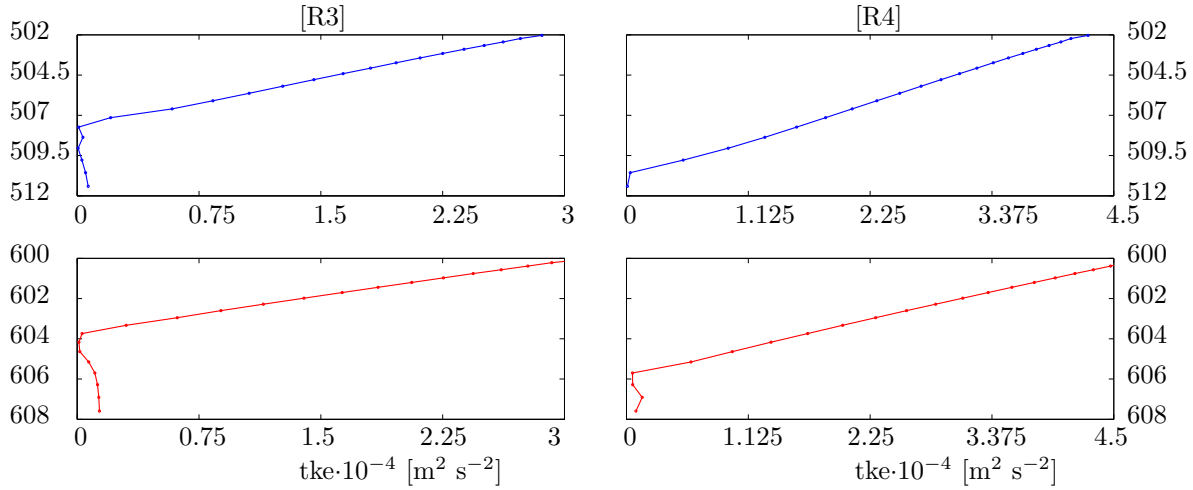

Figure 31: Vertical profile of the upper layers of turbulent kinetic energy at d1 (blue curve) and d2 (red curve) for [R3] on the left and [R4] on the right. Z-axises correspond to depth in meters. The z-axis labels are omitted in the plot to allow for higher resolution of the figure.

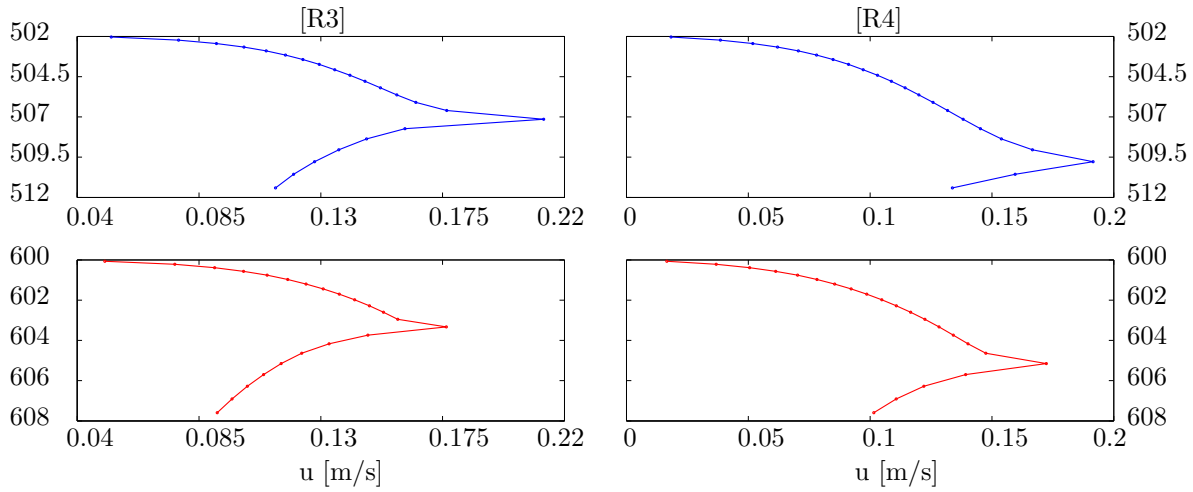

Figure 32: Vertical profile of the upper layers of u velocities at d1 (blue curve) and d2 (red curve) for [R3] on the left and [R4] on the right. Z-axises correspond to depth in meters. The z-axis labels are omitted in the plot to allow for higher resolution of the figure.

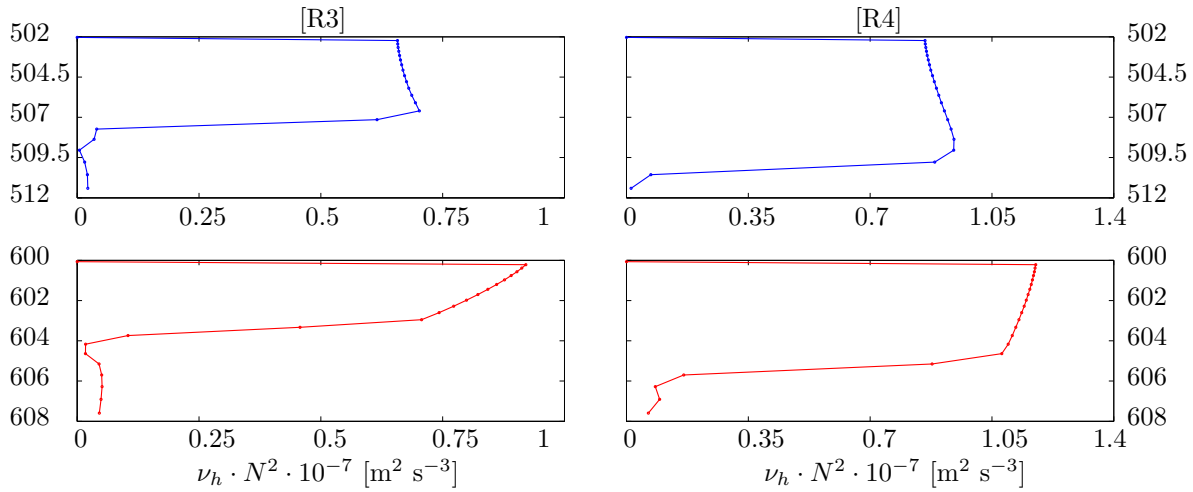

Figure 33: Vertical profile of the upper layers of the buoyancy flux ($\nu_h \cdot N^2$) at d1 (blue curve) and d2 (red curve) for [R3] on the left and [R4] on the right. Z-axises correspond to depth in meters. The z-axis labels are omitted in the plot to allow for higher resolution of the figure.

4.3 Conclusions

It is shown that a module parameterizing melting rates, salinity and heat fluxes is successfully integrated into GETM. The basic characteristics of the ice pump are reproduced and dependencies of melting rate, salinity and heat fluxes on key parameters are investigated, with the following conclusions:

- Vertical resolution is a major factor determining melting rates, especially near the grounding line. It is not obvious if an increased resolution leads to more realistic results or if different melting rates are outcomes of an insufficient parameterization, due to lack of observational evidence.
- Increased surface roughness leads to thicker melt water plumes and increased entrainment, hence greater melting rates.
- Increased entrainment leads to greater sensibility of the melting rates towards the ambient cavern water properties.
- In regimes where the slope is roughly equivalent with the drag coefficient, melt water plume thickness is decreased (ignoring effects from Coriolis forces).

A comparison with the cavern water properties of PIIS, sampled by an AUV[21] shows mixing of ISW near the grounding line inside the cavern. This difference to the produced model runs could be explained by known processes in Antarctic ice shelf caverns, that are not included in the model, such as tidal induced mixing, the influence of the Coriolis force and SFW discharge at the grounding line. Further known processes that are not included are the effects of frazil production in supercooled ISW and the cavern geometries are heavily idealized and calculated in a 2D-domain. Little attention is paid to the ambient water mass and correct parameterization of realistic in- and outflow conditions near the calving front. It is known from other models, such as plume models[20] or box models[34], that calculated melting rates near grounding lines are usually overestimates. Reduced melting rates in that region, caused by high vertical resolution, could imply a need for increased vertical resolution towards the ice shelf draft of Ocean General Circulation Models.

5 Table of parameters and constants

Table 3: Parameters and constants

Symbol	Units	Parameter
A		air saturation fraction
$c_{(0,1,...,27)}$		various fitting constants
C_d		drag coefficient
c_I	J $^\circ$C^{-1} Kg^{-1}	specific heat capacity of ice
c_w	J $^\circ$C^{-1} Kg^{-1}	specific heat capacity of seawater
D	m	ice shelf thickness
d	m	distance from the boundary
L	J Kg^{-1}	latent heat of fusion
m	m s^{-1}	melting rate
p	dbar	pressure at the ice shelf draft
S_A	g Kg^{-1}	Absolute Salinity
S_b	psu	salinity of the interfacial sublayer
S_p	psu	practical salinity
S_w	psu	salinity of the well mixed parts in the boundary layer
T_b	$^\circ$C	temperature of the interfacial sublayer
T_f	$^\circ$C	freezing temperature of seawater
T_I	$^\circ$C	temperature of the inner parts of the ice shelf
T_w	$^\circ$C	temperature of the well mixed parts in the boundary layer
U	m s^{-1}	free stream velocity
u_*	m s^{-1}	friction velocity
z'	m	distance between boundary and nearest vertical grid point
z_0	m	surface roughness length
z_0^s	m	surface roughness feature scale
Γ_S		salt transfer coefficient
γ_S	m s^{-1}	salt transfer velocity
Γ_T		heat transfer coefficient
γ_T	m s^{-1}	heat transfer velocity
κ		Kármán's constant
κ_I	m^2 s^{-1}	heat diffusion coefficient of ice
λ	$^\circ$	longitude
λ_1	$^\circ$C	salinity coefficient
λ_2	$^\circ$C	interpolation coefficient
λ_3	$^\circ$C dbar^{-1}	pressure coefficient
μ^I	J mol^{-1}	chemical potential of ice
μ^W	J mol^{-1}	chemical potential of water in seawater
ρ_I	Kg m^{-3}	reference density of ice
ρ_w	Kg m^{-3}	reference density of seawater
ϕ	$^\circ$	latitude
ϕ_B^S	Kg m^{-2} s^{-1}	turbulent salt flux through the boundary layer
ϕ_B^T	W m^{-2}	turbulent heat flux through the boundary layer
ϕ_I^T	W m^{-2}	conductive heat flux through the ice shelf
ϕ_M^S	Kg m^{-2} s^{-1}	melting/freezing salt flux
ϕ_M^T	W m^{-2}	latent heat flux

6 Acronyms

Table 4: Acronyms

Antarctic ice shelves, as illustrated in fig. 1.	
ABB	Abbot ice shelf
AMY	Amery ice shelf
BRL	Brunt and Riiser-Larsen ice shelf
FIL	Filchner ice shelf
FIM	Fimbulisen ice shelf
GEO	George VI ice shelf
GTZ	Getz ice shelf
LAR	Larsen C ice shelf
PIIS	Pine Island ice shelf
RON	Ronne ice shelf
ROS	Ross ice shelf
SHA	Shackleton ice shelf
WE	West ice shelf
Water bodies	
AABW	Antarctic Bottom Water
ISW	Ice Shelf Water
HSSW	High Salinity Shelf Water
CDW	Circumpolar Deep Water
SFW	subglacial freshwater
Other	
AUW	autonomous underwater vehicle
CDT	Conductivity-Temperature-Depth
GETM	General Estuarine Transport Model
GOTM	General Ocean Turbulence Model
IHB	International Hydrographic Bureau
IHO	International Hydrographic Organization
POLAIR	Polar Ocean Land Atmosphere and Ice Regional

A Appendix: Calculating the melting rate according to Millero

Shorten (16) to:

$$T_b = \lambda_1 S_b + \underbrace{\lambda_2 + p\lambda_3}_{\epsilon_3} = \lambda_1 S_b + \epsilon_3 \tag{33}$$

Solve (21) for the melting rate m:

$$m = \frac{-\rho_w u_* \Gamma_S (S_b - S_w)}{\rho_I S_b} \tag{34}$$

Insert (34) in (20) and solve for 0:

$$\begin{aligned}
0 &= \overbrace{\rho_w u_* \Gamma_S}^{\epsilon_1} L \frac{S_b - S_w}{S_b} - c_I \overbrace{\rho_w u_* \Gamma_S}^{\epsilon_1} \frac{S_b - S_w}{S_b}(T_I - T_b) - \overbrace{\rho_w c_w u_* \Gamma_T}^{\epsilon_2}(T_b - T_w) \\
0 &= \epsilon_1 L \frac{S_b - S_w}{S_b} + c_I \epsilon_1 \frac{S_b - S_w}{S_b}(T_b - T_I) + \epsilon_2 (T_w - T_b) \qquad /*S_b \\
0 &= \epsilon_1 L S_b - \epsilon_1 L S_w + c_I \epsilon_1 S_b T_b - c_I \epsilon_1 S_b T_I - c_I \epsilon_1 S_w T_b + c_I \epsilon_1 S_w T_I + \epsilon_2 S_b T_w - \epsilon_2 S_b T_b
\end{aligned} \tag{35}$$

Insert (33) in (35):

$$\begin{aligned}
0 = S_b^2 \overbrace{(c_I \epsilon_1 \lambda_1 - \epsilon_2 \lambda_1)}^{\epsilon_4} + Sb \overbrace{(\epsilon_1 L + c_I \epsilon_1 \epsilon_3 - c_I \epsilon_1 T_I - c_I \epsilon_1 S_w \lambda_1 + \epsilon_2 T_w - \epsilon_2 \epsilon_3)}^{\epsilon_5} \\
+ \underbrace{(-\epsilon_1 L S_w - c_I \epsilon_1 \epsilon_3 S_w + c_I \epsilon_1 S_w T_I)}_{\epsilon_6} \\
0 = S_b^2 \epsilon_4 + S_b \epsilon_5 + \epsilon_6
\end{aligned} \tag{36}$$

Solve quadratic equation (36):

$$S_{b1/2} = \frac{-\epsilon_5 \pm \sqrt{\epsilon_5^2 - 4\epsilon_4 \epsilon_6}}{2\epsilon_4}$$

With the neglect of negative salinities, this leads to one solution with:

$$S_b = S_b(S_w, T_w, p, T_I, u_*) \tag{37}$$

(37) can now be used to calculate the freezing temperature T_b from (16) and then the melting rate m from (34). This does suffice to calculate the heat and salt fluxes (1),(2) at the ice-ocean interface.

B Appendix: Calculating the melting rate according to TEOS-10

Rewrite (35) to:

$$\begin{aligned} 0 &= \overbrace{\epsilon_1 L S_b - \epsilon_1 L S_w - c_I \epsilon_1 S_b T_I + c_I \epsilon_1 S_w T_I + \epsilon_2 S_b T_w}^{\xi_1(S_b)} + T_b \overbrace{(c_I \epsilon_1 S_b - c_I \epsilon_1 S_w - \epsilon_2 S_b)}^{\xi_2(S_b)} \\ 0 &= \frac{\xi_1(S_b)}{\xi_2(S_b)} + T_b \end{aligned} \tag{38}$$

With $S_p = S_b$ (18) can be written as:

$$\begin{aligned} S_A &= \overbrace{\frac{35.16504\text{g Kg}^{-1}}{35}}^{\xi_3} S_b + \overbrace{\delta S_A(\phi, \lambda, p)}^{\xi_4} \\ S_A &= \xi_3 S_b + \xi_4 \end{aligned} \tag{39}$$

Insert (19) in (38), with $T_f = T_b$ and (39):

$$\begin{aligned} 0 &= \frac{\xi_1(S_b)}{\xi_2(S_b)} + T_f(S_A(S_b, \delta S_A(\lambda, \phi, p)), p) \\ 0 &= \frac{\epsilon_1 L S_b - \epsilon_1 L S_w - c_I \epsilon_1 S_b T_I + c_I \epsilon_1 S_w T_I + \epsilon_2 S_b T_w}{c_I \epsilon_1 S_b - c_I \epsilon_1 S_w - \epsilon_2 S_b} + c_0 \\ &\quad + c_{23}(\xi_3 S_b + \xi_4)(c_1 + (c_{23}(\xi_3 S_b + \xi_4))^{(1/2)}(c_2 + (c_{23}(\xi_3 S_b + \xi_4))^{(1/2)} \\ &\quad \cdot(c_3 + (c_{23}(\xi_3 S_b + \xi_4))^{(1/2)}(c_4 + (c_{23}(\xi_3 S_b + \xi_4))^{(1/2)}(c_5 + c_6(c_{23}(\xi_3 S_b + \xi_4))^{(1/2)}))))) \\ &\quad + c_{24} p(c_7 + c_{24} p(c_8 + c_9 c_{24} p)) \\ &\quad + c_{23}(\xi_3 S_b + \xi_4) c_{24} p(c_{10} + c_{24} p(c_{12} + c_{24} p(c_{15} + c_{21} c_{23}(\xi_3 S_b + \xi_4)))) \\ &\quad + c_{23}(\xi_3 S_b + \xi_4)(c_{13} + c_{17} c_{24} p + c_{19} c_{23}(\xi_3 S_b + \xi_4)) \\ &\quad + (c_{23}(\xi_3 S_b + \xi_4))^{(1/2)}(c_{11} + c_{24} p(c_{14} + c_{18} c_{24} p) \\ &\quad + c_{23}(\xi_3 S_b + \xi_4)(c_{16} + c_{20} c_{24} p + c_{22} c_{23}(\xi_3 S_b + \xi_4)))) \\ &\quad - c_{25} A \left(c_{26} - \frac{\xi_3 S_b + \xi_4}{c_{27}} \right), \end{aligned} \tag{40}$$

with $c_{(0,1,\ldots,27)}$ being constants, A the saturation fraction of dissolved air in seawater and $\epsilon_{(1,2)}$ see (35). Equation (40) is the equivalent of (36), i.e. S_b must be determined all other parameters are constants. Once S_b is computed the freezing temperature T_b can be calculated from (19) and the melting rate m from (34).

C Appendix: Derivation of gravity current formulas

Vertical integration of (26) with the velocity being subject to the boundary condition

$$u = v = 0 \begin{cases} z = z_b \\ z = z_i \end{cases},$$

and the following integration relations

$$\begin{aligned} G'H &= \int_{z_b}^{z_i} g \frac{\rho - \rho_0}{\rho_0} dz \\ UH &= \int_{z_b}^{z_i} u dz \\ VH &= \int_{z_b}^{z_i} v dz \end{aligned}$$

with G' being the reduced gravity acceleration and the layer depth H, leads to

$$\begin{aligned} \frac{\partial UH}{\partial t} - f'VH &= G'HS_x - \frac{\tau_x}{\rho_0} \\ \frac{\partial VH}{\partial t} + f'UH &= -\frac{\tau_y}{\rho_0}. \end{aligned} \tag{41}$$

The shear stresses $\tau_{x,y}$ at the ice shelf base are parameterized by usage of a quadratic friction law

$$\begin{aligned} \frac{\tau_x}{\rho_0} &= C_d \left|\mathbf{U}\right| U \\ \frac{\tau_y}{\rho_0} &= C_d \left|\mathbf{U}\right| V \end{aligned}$$

with $|\mathbf{U}| = \sqrt{U^2 + V^2}$ and the drag coefficient C_d, so (41) can be written as

$$\begin{aligned} \frac{\partial U}{\partial t} H + \frac{\partial H}{\partial t} U - f'VH &= G'HS_x + C_d \left|\mathbf{U}\right| U \\ \frac{\partial V}{\partial t} H + \frac{\partial H}{\partial t} V + f'UH &= C_d \left|\mathbf{U}\right| V. \end{aligned} \tag{42}$$

In the one-dimensional case the entrainment velocity is defined as

$$w_E = \frac{\partial H}{\partial t},$$

and the non-dimensional entrainment parameter is defined as

$$E = \frac{w_E}{|\mathbf{U}|}. \tag{43}$$

Inserting (43) into (42) leads to

$$\begin{aligned}\frac{\partial U}{\partial t} - f'V &= G'S_x - \frac{C_d\,|\mathbf{U}|\,U}{H} - \frac{\partial H}{\partial t}\frac{U}{H} \\ &= G'S_x - \frac{|\mathbf{U}|\,U}{H}\,(C_d + E) \\ \frac{\partial V}{\partial t} + f'U &= -\frac{C_d\,|\mathbf{U}|\,V}{H} - \frac{\partial H}{\partial t}\frac{V}{H} \\ &= -\frac{|\mathbf{U}|\,V}{H}\,(C_d + E)\end{aligned} \tag{44}$$

Arneborg et al.[1] argue that for subcritical flows the entrainment parameter is much smaller than the drag coefficient and when assuming quasigeostrohpic flows the acceleration can be neglected, so (44) can be reduced to

$$\begin{aligned}f'V &= -G'S_x + \frac{|\mathbf{U}|\,U}{H}C_d \\ f'U &= -\frac{|\mathbf{U}|\,V}{H}C_d,\end{aligned}$$

which is

$$f'\begin{pmatrix}V\\U\end{pmatrix} = -G'\begin{pmatrix}S_x\\0\end{pmatrix} + \frac{C_d\,|\mathbf{U}|}{H}\begin{pmatrix}U\\-V\end{pmatrix} \tag{45}$$

in vector form.

The coordinate system $\begin{pmatrix}x\\y\end{pmatrix} \rightarrow \begin{pmatrix}x'\\y'\end{pmatrix}$ is being rotated by the angle β such that x' is parallel and y' is perpendicular to the direction of the flow, see fig. 34. The slope S_{ice} and velocity $\vec{U}$ with its components U, V therefore change to

$$\begin{aligned}\begin{pmatrix}S_x\\0\end{pmatrix} &\rightarrow \begin{pmatrix}S_x\sin(\beta)\\S_x\cos(\beta)\end{pmatrix} = \begin{pmatrix}S_{x'}\\S_{y'}\end{pmatrix} \\ \begin{pmatrix}U\\V\end{pmatrix} &\rightarrow \begin{pmatrix}U\cos(\beta) + V\sin(\beta)\\0\end{pmatrix} = \begin{pmatrix}U'\\V'\end{pmatrix}\end{aligned} \tag{46}$$

respectively, with the absolute value of the velocity being rotational invariant, i.e. $|\mathbf{U}| = |\mathbf{U}'|$.

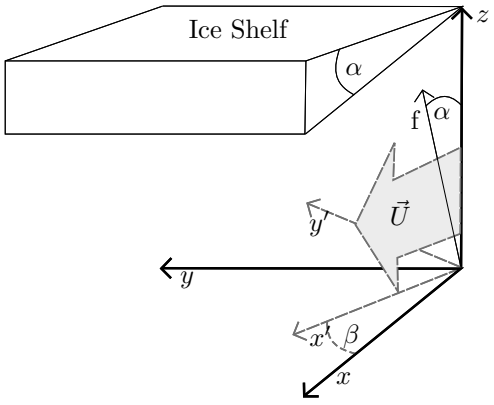

Figure 34: The used coordinate system in 3 and Appendix C. The z-axis is parallel to the normal vector of the ice shelf, therefore the Coriolis parameter is a projection on the z-Axis. The x-axis is parallel to the slope of the ice shelf $S_x = \tan(\alpha)$ and x' is parallel to integrated mean flow $\vec{U}$, with β being the deflection angle of the flow due to influence of Coriolis terms in (26). The slope of the flow S'_{ice} is a projection of S_x onto x' and y' and $\vec{U'}$ is the projection of the velocity components U and V onto x' as described in (46).

Equation (45) can thus be written as

$$f' \begin{pmatrix} 0 \\ U' \end{pmatrix} = -G' \begin{pmatrix} S_x \sin(\beta) \\ S_x \cos(\beta) \end{pmatrix} + \frac{C_d \left|\mathbf{U}\right|}{H} \begin{pmatrix} U' \\ 0 \end{pmatrix},$$

which translates to

$$\begin{aligned} G' S_x \sin(\beta) &= \frac{\left|\mathbf{U}\right|^2}{H} C_d \\ G' S_x \cos(\beta) &= -f' \left|\mathbf{U}\right| \end{aligned} \tag{47}$$

in component form, with the usage of the relation $|\mathbf{U}'| = \sqrt{U'^2 + V'^2} = U'$. Dividing the upper equation (47) with the lower equation (47) yields the Ekman number in accordance with Arneborg et al.[1]:

$$K = \tan(\beta) = -\frac{|\mathbf{U}|}{H f'} C_d. \tag{48}$$

The slope of the mean flow can be written as $S_{x'} = \tan(\alpha') = S_x \sin(\beta)$ with α' being the velocity slope angle, similar to the bottom slope angle $S_x = \tan(\alpha)$. Inserting this relation into a non-dimensionalized upper equation (47) yields the Froude number:

$$Fr^2 = \frac{\tan(\alpha')}{C_d} = \frac{\left|\mathbf{U}\right|^2}{G' H}. \tag{49}$$

In case of no deflection of the mean flow due the Coriolis forces, i.e. $f = 0$, equation (45) leads to

$$Fr^2 = \frac{\tan(\alpha)}{C_d} = \frac{U^2}{G' H}.$$

The relation between the Froude and Ekman number can be found by inserting (48) into (49):

$$\begin{aligned} Fr &= \sqrt{\frac{\tan(\alpha)\sin(\beta)}{C_d}} \\ &= \sqrt{\frac{\tan(\alpha)\sin(\arctan(K))}{C_d}} \end{aligned} \tag{50}$$

and using the relation

$$\sin(\arctan(K)) = \frac{K}{\sqrt{K^2 + 1}},$$

leads to

$$Fr = \sqrt{\frac{\tan(\alpha) K}{C_d \sqrt{K^2 + 1}}}.$$

An alternative form of the Ekman number can be found by solving (49) for

$$|\mathbf{U}| = \sqrt{G' H} Fr$$

and inserting this into (48), yields

$$\begin{aligned} K &= -\frac{C_d}{f'H}\sqrt{G'H}Fr \\ &= -\frac{C_d}{f'}\sqrt{\frac{G'}{H}}Fr. \end{aligned} \tag{51}$$

Equation (51) can be rewritten as

$$\frac{G'}{H} = \left(\frac{f'}{C_d}\frac{K}{Fr}\right)^2.$$

D Appendix: The ice shelf module – Structure and procedure

The `ice_shelf` module contains 4 public variables,

- `is_fluxes`: A logical variable which controls the usage of the module within GETM.
- `Flux_T`: The 2D temperature flux field.
- `Flux_S`: The 2D salinity flux field.
- `melting`: The 2D melting rate field.

and 2 subroutines:

- `init_ice_shelf`: Assigns initial values to options and parameters and reads from `get.inp`, as well as allocating and initializing `Flux_T`, `Flux_S` and `melting`.
- `do_ice_shelf`: A wrapper around the main subroutines, needed to calculate the melting rate, heat and salinity fluxes.

A list of options and variables read from `get.inp` is provided in table 5. The remaining variables are stored in the `ice_shelf_variables` module and auxiliary subroutines that are called in `do_ice_shelf` are stored within their respective files, see table 6. The calculation of δS_A requires it's own set of coordinates `lat_ice` and `lon_ice`, because the `gsw_oceanographic_toolbox` could falsely interpret coordinates near Antarctic ice shelf grounding lines as land coordinates; hence, it is suggested to use coordinates well within the Southern Ocean near the calving front of the respective ice shelf. The subroutine `do_ice_shelf` employs the following procedure (minor details are omitted):

- iteration over the horizontal grid and the land-sea mask `az(i,j)`
- save input arrays as a corresponding `REALTYPE`, e.g. `S(i,j)` = `Sw`
- if the surface friction velocity is zero, set `melting(i,j)`, `Flux_T(i,j)` and `Flux_S(i,j)` to zero and continue the iteration.
- if the surface friction velocity is unequal zero use the chosen freezing point calculation method:
  - `Tfmethod` = 0 calculate melting rate, heat and salt flux using to the linearized version of Millero [30]
  - `Tfmethod` = 1 according to TEOS-10 use the `gsw_oceanographic_toolbox` and:
    - convert `Tw` and `Sw` to Conservative Temperature and Absolute Salinity respectively
    - check the chosen zero finding method and choose the proper subroutine `find_root_brent` or `find_root_zhang`
    - reconvert `Tw`, `Sw` and the computed `Sb` and `Tb` to practical salinity and potential temperature
  - set `melting(i,j)`, `Flux_T(i,j)` and `Flux_S(i,j)` to the calculated corresponding `REALTYPEs`, e.g. `melting(i,j)` = `m`
  - if `sanity` is true and errors are encountered, display debug message and stop program

The module aborts the program if the surface salinity is below $T_w < 0.12$, if any of the zero finding algorithms exceed the maximum amount of iterations or no salinity of the interfacial sublayer can be found for $0.12 \leq S_b \leq 45$. The initial bracket is set to 35 and expanded, if necessary. The temperature of the ice shelf surface T_I is not an aquatic temperature and therefore not included in the conversion to Conservative Temperature; therefore, there are difference between the right and left hand side of equation (20), especially in case of low melting rates. Thus, the heat flux is calculated using

$$\phi_B^T = \rho_w c_w u_* \Gamma_T (T_b - T_w).$$

This discrepancy could be solved by converting and reconverting T_I as well, although doing so would be a physical inconsistent interpretation of the variable.

Table 5: `ice_shelf` options and input variables (all public)

name	type	explanation
`is_fluxes`	`logical`	controls usage of the `ice_shelf` module
`sanity`	`logical`	displays debug message and terminates GETM, if an error is encountered
`Tfmethod`	`integer`	determines freezing point calculation: [0] linearized version of Millero[30], [1] TEOS-10
`saar_const`	`logical`	chooses whether δS_A is calculated or set to a constant
`saar`	`REALTYPE`	constant value of δS_A
`saturation_fraction`	`REALTYPE`	saturation fraction of dissolved air in seawater
`Ti`	`REALTYPE`	ice shelf surface or core temperature
`lat_ice`	`REALTYPE`	latitude used for calculation of δS_A
`lon_ice`	`REALTYPE`	longitude used for calculation of δS_A
`eps`	`REALTYPE`	accuracy of convergence used by the zero finding algorithms
`itermax`	`integer`	maximum amount of iterations of the zero finding algorithms
`zero_method`	`integer`	determines zero finding algorithm: [0] Zhang[46], [1] Brent's method[46]

Table 6: auxiliary subroutines and functions

name	description
`conversion`	converts T_w, S_w and calculates L according to TEOS-10
`find_root_brent`	Brent's method[46], zero finding algorithm
`find_root_zhang`	zero finding algorithm according to Zhang[46]
`fluxesMillero`	calculates melting rate, temperature and salinity fluxes using a linearized version of Millero[30]
`gsw_oceanographic_toolbox`	TEOS-10 function library
`melting_fluxes`	calculates melting rate, temperature and salinity fluxes in case of using TEOS-10
`reconversion`	reconverts T_w, T_b, S_w and S_b
`do_sanity`	displays occurring errors and aborts program
`sublayer_function`	the function that needs to be solved for 0 to calculate S_b
`swap_real`	swaps two `REALTYPE`s

D.1 Integration in GETM

The integration of the `ice_shelf` module is done in a similar fashion to the `meteo` and other optional modules. The initialization is called near the start of the program within the `initialise` module and is mainly responsible for reading variables and settings from the `get.inp` file. A crucial setting is the variable `is_fluxes`, which determines if the call of `do_ice_shelf` within the `integration` module happens, i.e. `is_fluxes` is responsible for turning the `ice_shelf` module on or off. The actual calculations are done in the `do_ice_shelf` subroutine, which requires the temperature and salinity surface fields, i.e. `(i,j,k` = `kmax)`, the normalized surface stress at the T-points `taus`, the elevation `z` and the timestep `n`. `do_ice_shelf` calculates the 2D-fields of the temperature and salinity fluxes `Flux_T`, `Flux_S` which are used by the respective tracer equations `do_temperature` and `do_salinity`. Name and location of relevant modules and subroutines are listed in table 7 and fig. 35 pictures the integration of the ice_shelf module in GETM. The melting rate field `melting` is only saved as output and not used by other modules. A note of importance: The salinity fluxes are used within the advection and diffusion of the salinity field. The elevation (in this case the ice shelf draft) is treated as conservative and is not modified by the melting rate. This is done, because the horizontal advection of the ice shelf influences the draft as well e.g. a fast moving ice shelf could increase the draft, even for regimes with melting.

Table 7: GETM structure

name of module	location
`ice_shelf`	`src/iceshelf/ice_shelf.F90`
`meteo`	`src/meteo/meteo.F90`
`initialise`	`src/getm/initialise.F90`
`integration`	`src/getm/integration.F90`
`m3d`	`src/3d/m3d.F90`
name of subroutine	location
`init_ice_shelf`	`src/iceshelf/ice_shelf.F90`
`do_ice_shelf`	`src/iceshelf/ice_shelf.F90`
`do_temperature`	`src/3d/temperature.F90`
`do_salinity`	`src/3d/salinity.F90`

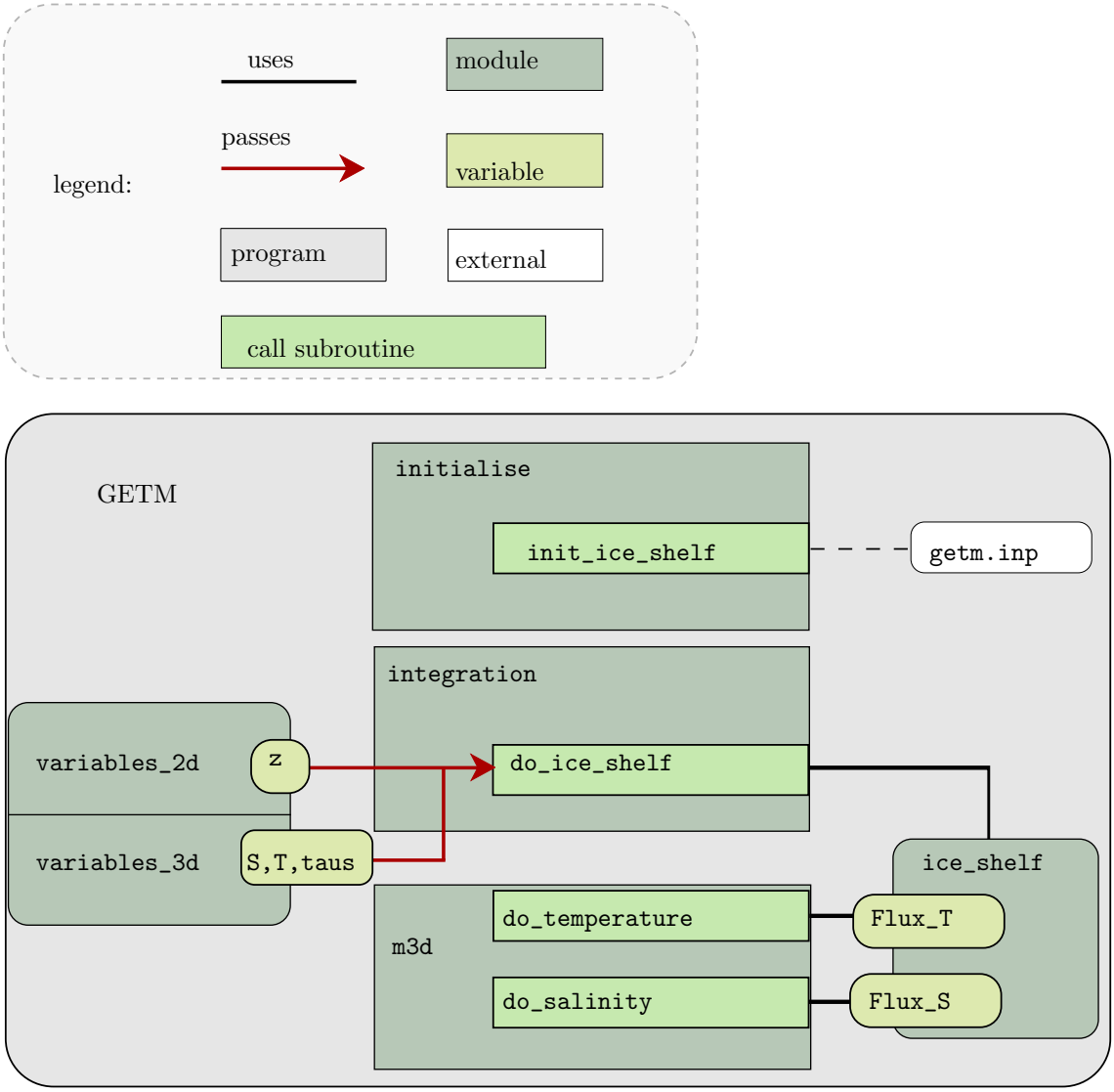

Figure 35: Integration of the ice shelf module into GETM: The displayed modules are the ones responsible for the calls of the pictured subroutines, e.g. the `do_salinity` subroutine is included in the `salinity` module, but is called in `m3d`. The 3D variables T and S are passed as 2D-fields with `k = kmax`, i.e. only the surface values are used by `do_ice_shelf`. Not shown is the additional pass of the timestep `n` (a local variable of the `integration` module) to `do_ice_shelf`, which was only done for debugging purposes during development.

D.2 Additional changes to GETM

To run GETM as a slice model while using the `ice_shelf` module, there are several necessary changes needed for GETM:

1 Nudging of the 3D salinity and temperature fields to provide in- and outflow conditions at the calving line.
2 Changing the equation of state to take increased pressure from the elevation profile (the ice shelf draft) into account.
3 Adding surface roughness parameterization, similar to that of the bottom roughness.
4 Obeying the the rigid lid condition.

[1] Nudging of the 3D tracer fields for salinity and temperature is done by providing four additional profiles to the temperature and salinity routines. Each tracer field T_{racer} requires a profile including the nudging data T_{nudge} and another profile containing the relaxation times T_{relax}. The tracer field is then nudged by iterating over the horizontal grid, the land-sea mask and vertical grid and computing

$$\begin{aligned} T_{racer}(i,j,k) = (1 - T_{relax}(i,j,k))\, T_{racer}(i,j,k) \\ + T_{relax}(i,j,k)\, T_{nudge}(i,j,k), \end{aligned}$$

similar to the implementation of the salt-wedge test. Proper implicit nudging could be implemented by writing nudging terms into the advection and vertical diffusion, i.e the lines

$$\begin{aligned} a2(k) &= a2(k) + hn(i,j,k)\, dt\, T_{relax}(i,j,k)^{-1} \\ a4(k) &= a4(k) + hn(i,j,k)\, dt\, T_{nudge}(i,j,k)\, T_{relax}(i,j,k)^{-1}, \end{aligned}$$

have to be added for surface ($k = k_{max}$), inner ($1 < k < k_{max}$) and bottom ($k = 1$) layers. Due to ease of use, the upper version is currently implemented; although, the tracer equation for temperature has the second version included, albeit commented out. Currently only netCDF format is supported to import T_{nudge} and T_{relax} and the import options are added at the end of the respective tracer section in the `get.inp` file.
[2] The equation of state has to changed only slightly. Currently the pressure is calculated by adding the layer heights, but starting from $p = 0$, i.e. the code need to reflect the depth of the ice shelf draft and the pressure needs to start from $p =$ ice shelf draft(i,j).
[3] There are two principle changes needed to be made in order to implement a surface roughness parameterization as described in 2.3: First the surface stress has to be calculated similar to the bottom stress in `stresses.F90`. The main difference to the bottom stress, is usage of the surface drag coefficient and setting k to k_{max}. Secondly, each call of the calculation for the bottom drag coefficient has to be accompanied by a call calculating the surface drag coefficient.
[4] The rigid lid option was implemented by Knut Klingbeil and fulfills the marginal condition

$$\frac{\partial \eta}{\partial t} = \frac{\partial}{\partial x} \int_{\text{bottom}}^{\text{surface}} u dz - \frac{\partial}{\partial y} \int_{\text{bottom}}^{\text{surface}} v dz = 0.$$

A slice model setup ($v = 0$) reduces this condition further to

$$0 = \frac{\partial}{\partial x} \int_{\text{bottom}}^{\text{surface}} u dz. \tag{52}$$

References

1. Arneborg, Lars; Fiekas, Volker; Umlauf, Lars, and Burchard, Hans. Gravity Current Dynamics and Entrainment - A Process Study Based on Observations in the Arkona Basin. *Journal of Physical Oceanography*, Vol. 37:2094–2113, 2006.
   Cited on pages 24, 48, 49.

2. Burchard, Hans; Bolding, Karsten, and Umlauf, Lars. GETM Source Code and Test Case Documentation. 2011. http://www.getm.eu/data/getm/doc/getm-doc-stable.pdf.
   Cited on page 18.

3. Depoorter, M. A.; Bamber, J. L.; Griggs, J. A.; Lenaerts, J. T. M.; Ligtenberg, S. R. M.; van den Broeke, M. R, and Moholdt, G. Calving fluxes and basal melt rates of Antarctic ice shelves. *Nature*, Vol. 502:89–92, October 2013.
   Cited on pages 1, 4, 6.

4. Dutrieux, Pierre; De Rydt, Jan; Jenkins, Adrian; Holland, Paul R.; Ha, Ho Kyung; Lee, Sang Hoon; Steig, Eric J.; Ding, Qinghua; Abrahamsen, E. Povl, and Schröder, Michael. Strong Sensitivity of Pine Island Ice-Shelf Melting to Climatic Variability. *Science*, Vol. 343(6167):174–178, January 2014.
   Cited on page 6.

5. Fer, Ilker; Makinson, Keith, and Nicholls, Keith W. Observations of Thermohaline Convection adjacent to Brunt Ice Shelf. *Journal of Physical Oceanography*, Vol. 42:502–508, 2012.
   Cited on page 4.

6. Galton-Fenzi, B. K.; Hunter, J. R; Coleman, R.; Marsland, S. J., and Warner, R. C. Modeling the basal melting and marine ice accretion of the Amery Ice Shelf. *Journal of Geophysical Research*, Vol. 113, September 2012.
   Cited on page 6.

7. Hellmer, Hartmut H. and Olbers, Dirk J. A two-dimensional model for the thermohaline circulation under an ice shelf. *Antarctic Science*, 1(4):325–336, 1989. doi: 10.1017/S0954102089000490.
   Cited on pages 12, 14, 15, 16, 19, 21.

8. Hellmer, Hartmut H.; Kauker, Frank; Timmermann, Ralph; Determann, Jürgen, and Rae, Jamie. Twenty-first-century warming of a large Antarctic ice-shelf cavity by a redirected coastal current. *Nature*, Vol. 485, May 2012.
   Cited on page 1.

9. Holland, David M. and Jenkins, Adrian. Modeling Thermodynamic Ice-Ocean Interactions at the Base of an Ice Shelf. *Journal of Physical Oceanography*, Vol. 29:1787–1800, 1999.
   Cited on pages 12, 14, 15, 16, 17, 21, 22.

10. Holland, Paul R.; Jenkins, Adrian, and Holland, David M. The Response of Ice Shelf Basal Melting to Variations in Ocean Temperature. *Journal of Climate*, Vol. 21:2558–2572, 2008.
    Cited on pages 1, 4, 12, 19.

11. Humbert, Angelika. Vulnerable ice in the Weddell Sea. *Nature Geoscience*, Vol. 5, May 2012.
    Cited on page 1.

12. International Hydrographic Bureau, . Hydrographic Dictionary - Glossary of Electronic Chart Display and Information System Related Terms. *Chairman: Captain H.-P. Rohde*, Vol. 1, 1994. http://www.iho.int/iho_pubs/standard/S-32/S-32-eng.pdf.
    Cited on page 1.

13. International Hydrographic Bureau, . Circular Letter 55. *IHB File No. S3/7020*, 7 November 2001. http://www.iho.int/mtg_docs/circular_letters/english/2001/Cl55e.pdf.
Cited on page 1.

14. International Hydrographic Organization, . Limits of Oceans and Seas. *Special Publication No. 23, 4th Edition*, June 2002. http://www.iho.int/mtg_docs/com_wg/S-23WG/S-23WG_Misc/Draft_2002/Draft_2002.htm.
Cited on pages 1, 2.

15. IOC, SCOR, and IAPSO, . The international thermodynamic equation of seawater - 2010: Calculation and use of thermodynamic properties. *Intergovernmental Oceanographic Commission, Manuals and Guides No 56, UNESCO (English)*, page 196 pp., 2010.
Cited on pages 4, 19.

16. Jacobs, Stanley S.; Gordon, Arnold L., and Ardai, J. L. Jr. Circulation and Melting Beneath the Ross Ice Shelf. *Science*, Vol. 203(4379):439–443, February 1979.
Cited on page 1.

17. Jacobs, Stanley S.; Jenkins, Adrian; Giulivi, Claudia F., and Dutrieux, Pierre. Stronger ocean circulation and increased melting rates under Pine Island Glacier ice shelf. *Nature Geoscience*, Vol. 4:519–523, August 2011.
Cited on page 6.

18. Jenkins, Adrian. A One-Dimensional Model of Ice Shelf-Ocean Interaction. *Journal of Geophysical Research*, Vol. 96(No. C11):20671–20677, 1991.
Cited on pages 12, 16, 19.

19. Jenkins, Adrian. Convection-Driven Melting near the Grounding Lines of Ice Shelves and Tidewater Glaciers. *Journal of Physical Oceanography*, Vol. 41:2279–2294, December 2011.
Cited on page 4.

20. Jenkins, Adrian and Bombosch, Andreas. Modeling the effects of frazil ice crystals on the dynamics and thermodynamics of Ice Shelf Water plumes. *Journal of Geophysical Research*, Vol. 100(No. C4):6969–6981, 1995.
Cited on pages 12, 19, 42.

21. Jenkins, Adrian; Dutrieux, Pierre; Jacobs, Stanley S.; McPhail, Stephen D.; Perrett, James R.; Webb, Andrew T., and White, David. Observations beneath Pine Island Glacier in West Antarctica and implications for its retreat. *Nature Geoscience*, Vol. 40:468–472, June 2010.
Cited on pages 6, 42.

22. Jenkins, Adrian; Nicholls, Keith W., and Corr, Hugh F. J. Observation and Parameterization of Ablation at the Base of Ronne Ice Shelf, Antarctica. *Journal of Physical Oceanography*, Vol. 40: 2298–2312, 2010.
Cited on pages 4, 12, 14, 15, 17, 19, 20, 21, 22.

23. Kader, B. A. and Yaglom, A. M. Heat and mass transfer laws for fully turbulent wall flows. *International Journal of Heat and Mass Transfer*, Vol. 15(12):2329–2351, 1972. doi: 10.1016/0017-9310(72)90131-7.
Cited on page 16.

24. Kusahara, Kazuya; Hasumi, Hiroyasu., and Tamura, Takeshi. Modeling sea ice production and dense shelf water formation in coastal polynyas around East Antarctica. *Journal of Geophysical Research*, Vol. 115, October 2010.
Cited on page 4.

25. Lewis, E. L. and Perkin, R. G. Supercooling and Energy Exchange Near the Arctic Ocean Surface. *Journal of Geophysical Research*, Vol. 88(No. C12):7681–7685, 1983.
Cited on page 4.

26. Lu, Peng; Li, Zhijun; Chang, Bin, and Lepäranta, Matti. A parameterization of the ice-ocean drag coefficient. *Journal of Geophysical Research*, Vol. 116, 2011.
Cited on pages 18, 25.

27. McDougall, Trevor J. and Barker, Paul M. Getting started with TEOS-10 and the Gibbs Seawater (GSW) Oceanographic Toolbox. *SCOR/IAPSO WG127*, ISBN 978-0-646-55621-5:28 pp., 2011. http://www.teos-10.org/.
Cited on pages 4, 19, 20.

28. Miles G.; MaykutMcPhee, Gary A.; Morison James H. Dynamics and Thermodynamics of the Ice/Upper Ocean System in the Marginal Ice Zone of the Greenland Sea. *Journal of Geophysical Research*, Vol. 92(No. C7):7017–7031, 1987.
Cited on page 16.

29. McPhee, Miles G. Air-Ice-Ocean Interaction: Turbulent Ocean Boundary Layer Exchange Processes. *Springer*, ISBN 978-0-387-78334-5, 2008.
Cited on pages 15, 17, 18, 22, 23.

30. Millero, F. J. Eighth report of the Joint Panel on Oceanographic Tables and Standards; Annex 6: Freezing point of seawater. *Unesco technical papers in marine science*, pages 29–31, 1978.
Cited on pages 4, 19, 22, 51, 52.

31. Mueller, R. D.; Padman, L.; Dinniman, M. S.; Erofeeva, S. Y.; Fricker, H. A., and King, M. A. Impact of tide-topography interactions on basal melting of Larsen C Ice Shelf, Antarctica. *Journal of Geophysical Research*, Vol. 117, may 2012.
Cited on pages 1, 4.

32. Nicholls, K. W.; Pudsey, C. J., and Morris, P. Summertime water masses off the northern Larsen C Ice Shelf. *Geophysical Research Letters*, Vol. 31, May 2004.
Cited on page 6.

33. Nøst, Ole Anders and Foldvik, Arne. A model of ice-ocean interaction with application to the Filcher-Ronne and Ross Ice Shelves. *Journal of Geophysical Research*, Vol. 99(No. C7):14243–14254, 1994.
Cited on pages 12, 14, 19, 21.

34. Olbers, D.; Hellmer, H. H., and Buck, F. F. J. H. A data-constrained model for compatibility check of remotely sensed basal melting with the hydrography in front of Antarctic ice shelves. *The Cryosphere Discussions*, Vol. 8(1):919–951, 2014.
Cited on page 42.

35. Robin, Gordon de Quetteville. FORMATION, FLOW, AND DISINTEGRATION OF ICE SHELVES. *Journal of Glaciology*, Vol. 24(No. 90):259–271, 1979.
Cited on page 4.

36. Scheduikat, M. and Olbers, Dirk J. A one-dimensional mixed layer model beneath the ross ice shelf with tidally induced vertical mixing. *Antarctic Science*, Vol. 2(1):29–42, 1990.
Cited on page 12.

37. Schoof, Christian. Beneath a floating ice shelf. *Nature Geoscience*, Vol. 3:450–451, July 2010.
Cited on page 6.

38. Sirevaag, Anders. Turbulent exchange coefficients for the ice/ocean interface in case of rapid melting. *Geophysical Research Letters*, Vol. 36, February 2009.
Cited on page 15.

39. Smedsrud, Lars H. and Jenkins, Adrian. Frazil ice formation in an ice shelf water plume. *Journal of Geophysical Research: Oceans*, Vol. 109, March 2004.
Cited on pages 1, 4.

40. Smedsrud, Lars H.; Jenkins, Adrian; Holland, David M., and Nøst, Ole Anders. Modeling ocean processes below Fimbulisen, Antarctica. *Journal of Geophysical Research*, Vol. 111, January 2006.
Cited on page 6.

41. Steele, Michael; Mellor, George L., and Mcphee, Miles G. Role of the Molecular Sublayer in the Melting or Freezing of Sea Ice. *Journal of Physical Oceanography*, Vol. 19:139–147, 1989.
Cited on page 22.

42. Timmermann, Ralph; Le Brocq, Anne M; Deen, Tara J; Domack, Eugene W; Dutrieux, Pierre; Galton-Fenzi, Ben; Hellmer, Hartmut H; Humbert, Angelika; Jansen, Daniela; Jenkins, Adrian; Lambrecht, Astrid; Makinson, Keith; Niederjasper, Fred; Nitsche, Frank-Oliver; Nøst, Ole Anders; Smedsrud, Lars Henrik, and Smith, Walter. A consistent dataset of Antarctic ice sheet topography, cavity geometry, and global bathymetry. *Earth System Science Data*, Vol. 2(2):261–273, 2010. doi: 10.5194/essd-2-261-2010. http://doi.pangaea.de/10.1594/PANGAEA.741917?format=html.
Cited on pages 2, 3, 6, 7, 8, 9, 10, 11.

43. Ueda, Herbert T. and Garfield, Donald E. Deep core drilling at Byrd Station, antarctica. *International Symposium on Antarctic Glaciological Exploration*, pages 53–63, 1968.
Cited on page 12.

44. Welander, Pierre. Thermal oscillations in a fluid heated from below and cooled to freezing from above. *Dynamics of Atmospheres and Oceans*, 1:215–223, 1977.
Cited on page 15.

45. Winkelmann, R.; Levermann, A.; Martin, M. A., and Frieler, K. Increased future ice discharge from Antarctica owing to higher snowfall. *Nature*, Vol. 492, December 2012.
Cited on page 1.

46. Zhang, Zhengqui. An Improvement to the Brent's Method. *International Journal of Experimental Algorithms*, Vol. 2:21–26, 2011.
Cited on pages 30, 52.